Deeply Virtual Compton Scattering at 6 GeV

J.P. Chen, E. Chudakov, C. de Jager, J. Gomez, O. Hansen, J. Lerose, R. Michaels, J. Mitchell, A. Saha, B. Wojtsekhowski, et al.

Proposal to Jefferson Lab PAC 18

Deeply Virtual Compton Scattering At 6 GeV

J. P. Chen, E. Chudakov, C. de Jager, J. Gomez, J. LeRose, R. Michaels, J. Mitchell, N. Liyanage, A. Saha, B. Wojtsekhowski
Jefferson Laboratory

J. Berthot, P. Bertin, A. Deur, R. Di Salvo, Y. Roblin (co-spokesperson)
University Blaise Pascal/IN2P3

G. Dodge, C. E. Hyde-Wright, C. Jutier, F. Sabatié (co-spokesperson), L. Todor, P. Ulmer, L. Weinstein
Old Dominion University

W. Boeglin, P. Markowitz
Florida International University

J. Templon
University of Georgia

P. Gueye
Hampton University

T. Chang, A. M. Nathan
University of Illinois at Urbana-Champaign

R. de Leo, L. Lagamba
INFN Bari

M. Amarian, E. Cisbani, S. Frullani, F. Garibaldi, R. Iommi, M. Iodice, G. M. Urciuoli
INFN Roma-Sanita

M. Vanderhaeghen
Johannes Gutenberg Universität

D. W. Higinbotham
Massachusetts Institute of Technology

X. Jiang
Rutgers University

P.A.M. Guichon
DSM/DAPNIA/SPhN CEA Saclay

and

The Hall A Collaboration

(June 1, 2000)

Abstract

We propose a measurement of the Deep Virtual Compton Scattering process (DVCS) $ep \to ep\gamma$ in Hall A at Jefferson Lab with a 6 GeV beam. We are able to explore the onset of Q^2 scaling, by measuring a beam helicity asymmetry for Q^2 ranging from 1.5 to 2.5 GeV^2 at $x_B \approx 0.35$. At this kinematics, the asymmetry is dominated by the DVCS - Bethe-Heitler (BH) interference, which is proportional to the imaginary part of the DVCS amplitude amplified by the full magnitude of the BH amplitude. The imaginary part of the DVCS amplitude is expected to scale early. Indeed, the imaginary part of the forward Compton amplitude measured in deep inelastic scattering (via the optical theorem) scales at Q^2 as low as 1 GeV^2. If the scaling regime is reached, we will make an 8% measurement of the skewed parton distributions (SPD) contributing to the DVCS amplitude. Also, this experiment allows us to separately estimate the size of the higher-twist effects, since they are only suppressed by an additional factor $1/Q$ compared to the leading-twist term, and have a different angular dependence.

We use a polarized electron beam and detect the scattered electron in the HRSe, the real photon in an electromagnetic calorimeter (under construction) and the recoil proton in a shielded scintillator array (to be constructed). This allows us to determine the difference in cross-sections for electrons of opposite helicities. This observable is directly linked to the SPD's.

We estimate that 25 days of beam (600 hours) are needed to achieve this goal.

1 Introduction

The understanding of the structure of the nucleon is a fundamental topic. Despite having been studied during the past forty years, there are still many questions left unanswered. An example of such is the extensive debate over the spin structure of the nucleon ground state. Two kinds of electromagnetic observables linked to the nucleon structure have been considered so far. Electromagnetic form factors, first measured on the proton by Hoftstader [1] in the 1950's, then more recently on the neutron [2]. Weak form factors have been measured in parity violating experiments [3]. Another approach initiated in the late 60's [4] studies parton distribution functions via Deep Inelastic Scattering (DIS)[5], [6] and Drell-Yan processes [7].

Recently a new theoretical framework has been proposed, namely the Skewed Parton Distributions (SPD). They provide an intimate connection between the ordinary parton distributions and the elastic form factors and therefore contain a wealth of information on the quark-gluon structure of the nucleon.

The QCD factorization theorems [8, 9] have established that the SPD's can be measured via exclusive reactions in the so-called deep virtual limit (fixed Bjorken variable x_B, $Q^2 >> \Lambda^2_{QCD}$, $Q^2 >> -t$, $t = (p' - p)^2$, where p and p' correspond to the initial and recoil proton four-vectors respectively). These deep virtual processes include $ep \to ep\pi^0$, $ep \to en\pi^+$, $ep \to eN^*\gamma$ and $ep \to ep\gamma$, ... Of course, the connection between the SPD's and the deep virtual measurements is subject to the same kind of higher twist corrections as in the case of ordinary parton distributions and deep inelastic scattering.

The simplest exclusive process to study that can be described in terms of SPD's is the Deeply Virtual Compton Scattering (DVCS) , $ep \to ep\gamma$. We propose a measurement of DVCS in Hall A at Jefferson Lab with a 6 GeV beam, in a kinematical range where the DIS already scales. We will be able to explore the onset of scaling for several distinct observables in a Q^2 range of 1.5 to 2.5 GeV^2 at $x_B \approx 0.35$. Assuming we are in the scaling regime, we will also make an 8% measurement of the SPD contribution to the DVCS process.

We will use a polarized electron beam and detect the scattered electron in the HRSe, the real photon in an electromagnetic calorimeter (under construction) and the recoil proton in a shielded scintillator array (to be constructed). This will allow us to determine the difference in cross-section for electrons of opposite helicities. This observable is directly linked to the SPD's as it will be shown in Section 2.

2 Theory

The DVCS reaction $\gamma^* p \to \gamma p$ has become a subject of considerable new interest. This process can be measured in the exclusive electroproduction reaction $ep \to ep\gamma$ in deep inelastic scattering kinematics. Recently X. Ji [10], [11] suggested using DVCS to get information about a new class of parton distribution functions, which he called Off-Forward Parton Distributions (OFPD). These parton functions generalize the concept of the parton distributions found in DIS (Fig. 1). They describe off-diagonal matrix elements and can be interpreted as quark correlation functions, unlike the usual parton distributions which represent probabilities.

These OFPD's, also known as Skewed Parton Distributions (SPD) contain a wealth of information on the spin structure of the proton. In particular, it has been shown that there is a sum rule relating the SPD's to the total angular momentum (spin and orbital) carried by the quarks [10].

The DVCS amplitude can be factorized in a soft part containing the non-perturbative physics and described by the SPD's and a parton process, calculable via perturbative QCD (pQCD) [8, 9, 12]. This is depicted in Fig. 1b and because of its topology, is commonly called the handbag diagram. It exhibits a Bjorken type Q^2 scaling behavior at fixed $x_B = Q^2/(2p.q)$ and fixed invariant momentum transfer between the initial and scattered proton. The DVCS amplitude and the SPD's are defined in appendix A. It has been demonstrated that the QCD Q^2 evolution equations of the SPD's combine the Dokshitser-Gribov-Lipatov-Altarelli-Parisi (DGLAP) evolution [13] of usual parton distributions and

the Efremov-Radyushkin-Brodsky-Lepage (ERBL) evolution [14] of meson distribution amplitudes in contrast with the DIS case where only DGLAP occurs [11]. The radiative corrections to the handbag diagram in DVCS have been evaluated up to next-to-leading order [15] in α_s.

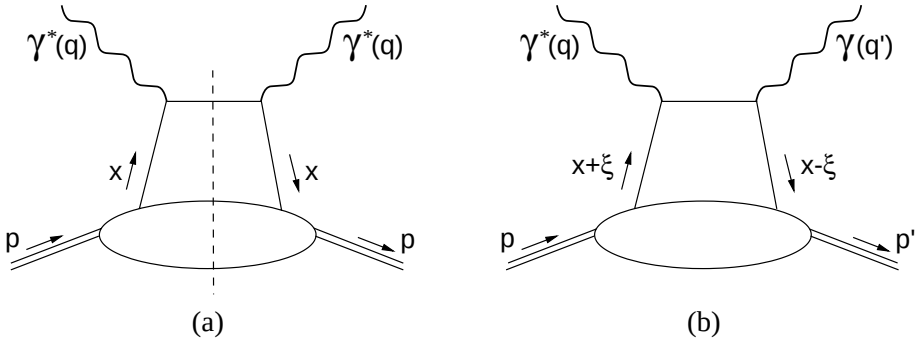

Figure 1: (a) Forward virtual Compton amplitude which describes the DIS cross-section via the optical theorem ($x_B = x$); (b) Handbag diagram occurring in the DVCS amplitude ($x_B = 2\xi/(\xi+1)$ at the deep virtual limit).

The deep inelastic scattering cross section is related to the forward Compton amplitude via the optical theorem. In the limit of DIS, this forward amplitude is dominated by the handbag diagram of Fig. 1a. On the other hand, the off-forward Compton amplitude of Fig. 1b directly describes the DVCS amplitude in the deeply virtual limit of large Q^2, large $s = (q+p)^2$ and small $t = (p'-p)^2$.

The momentum transfer to the proton $(p'-p)$ is characterized by two values: the invariant momentum transfer squared t, and the + component of the light cone momentum fraction ξ[10][1]: $\xi = (p-p')^+/P^+$, where $P = (p+p')/2$.

The extra degrees of freedom given by the t and ξ variables are what makes the dynamics of DVCS so rich and diverse. Depending on the kinematical domain, the SPD's can represent either the correlation between two quarks of momentum fractions $x+\xi$ and $x-\xi$, two antiquarks or between a quark and an antiquark (see Fig. 3).

A unique feature of DVCS is that by exploiting the interference between the DVCS and the Bethe-Heitler process where the real photon is radiated by the lepton, and which is completely calculable, it is possible to measure the real and imaginary part of the DVCS amplitude independently (Fig. 2). This fact has been known for a long time [16].

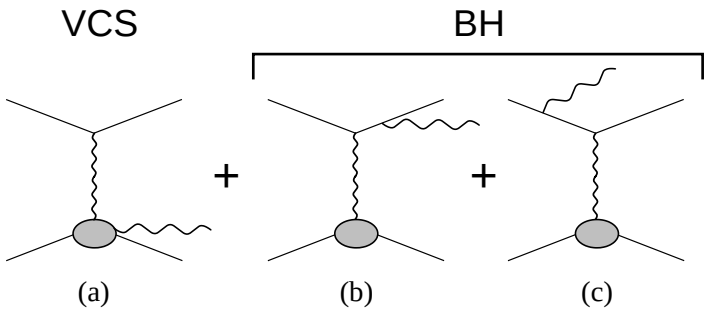

Figure 2: The DVCS process (a) along with the interfering Bethe-Heitler diagrams (b) and (c)

The helicity structure of DVCS is interesting in itself and gives rise to an angular dependence on the variable φ, the angle between the leptonic and hadronic planes. Diehl *et al.* [17] pointed out ways of using this structure to test the handbag diagram contribution to the DVCS amplitude.

[1]Other authors [12] use the alternate notation $\zeta = (p-p')^+/P^+$, but in this case, they refer to $P = p$.

The Q^2 at which the handbag dominance occurs can currently not be predicted from QCD. This is also true for DIS. At moderate Q^2, the higher twist corrections remain problematic in DIS as they are hard to disentangle from the leading term and its log behavior in Q^2. In the case of DVCS, we have the opportunity to gain detailed information on the size of these higher twists and determine the onset of scaling since each of the helicity amplitudes has a specific lowest twist.

The specific observable we propose to measure is the cross section difference for leptons of opposite helicities. This observable is non-zero only if the detected photon is out of the electron scattering plane. This cross-section difference is proportional to the interference of the imaginary part of the DVCS amplitude with a known BH weight.

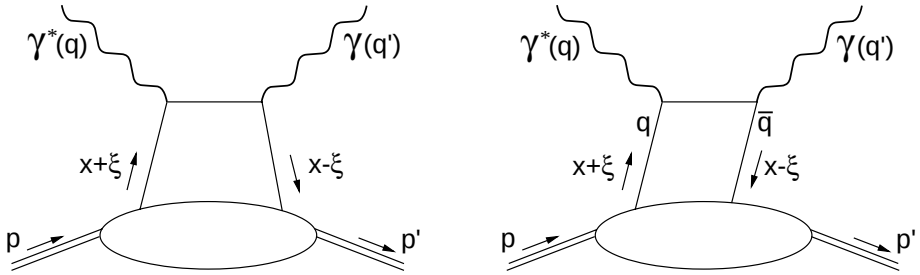

Figure 3: Dynamical behavior of the DVCS amplitude: a) q-q ($x+\xi$, $x-\xi>0$) or $\overline{q}$-$\overline{q}$ ($x+\xi$, $x-\xi<0$) distribution function; b) q-$\overline{q}$ correlation function ($x+\xi>0$, $x-\xi<0$). Unlike the DIS diagram of Fig. 1a, the DVCS amplitude also includes the crossed diagrams in which the virtual and real photons are exchanged.

The $\gamma^* p \to \gamma p$ subprocess can be described by 12 helicity amplitudes, among which 2 cancel out. The angular dependence in φ allows us to access these helicity amplitudes, and in particular separate those which are leading twist from those which are not. This gives us an additional handle to observe the onset of scaling. In the regime where the factorization is valid it will then be possible to extract some of the SPD distributions.

Finally, one must note that the cross-section difference is directly proportional to a linear combination of three SPD's at leading twist. Furthermore, because this observable is related to the imaginary part of the diagrams in Fig. 3, the amplitude is determined by the pole of the quark propagator. This cross-section difference is therefore determined by the SPD's evaluated at $x=\xi$ (just as the DIS measures parton distributions at $x=x_B$). This corresponds to the boundary between the two regimes shown in Fig. 3, namely between the ERBL and DGLAP evolutions. It is an essential feature of the proposed experiment, that we can measure this linear combination of SPD's at a specific kinematic point via the measurement of the imaginary part of the amplitude, and not a principal value integral over x present in the real part of the amplitude like in deep virtual meson electroproduction.

3 DVCS cross section and asymmetry

3.1 DVCS cross-section and SPD models

The full DVCS cross section has been computed at the leading twist in $1/Q$ taking into account the interference with the Bethe-Heitler [18], using some models for the SPD functions. These SPD models obey a number of constraints such as positivity bounds and parity considerations. Nevertheless there is still considerable freedom in constructing such models and several have been published [18, 19, 20, 21, 22, 23]. Figure 4 shows the DVCS cross-section computed using models from reference [18].

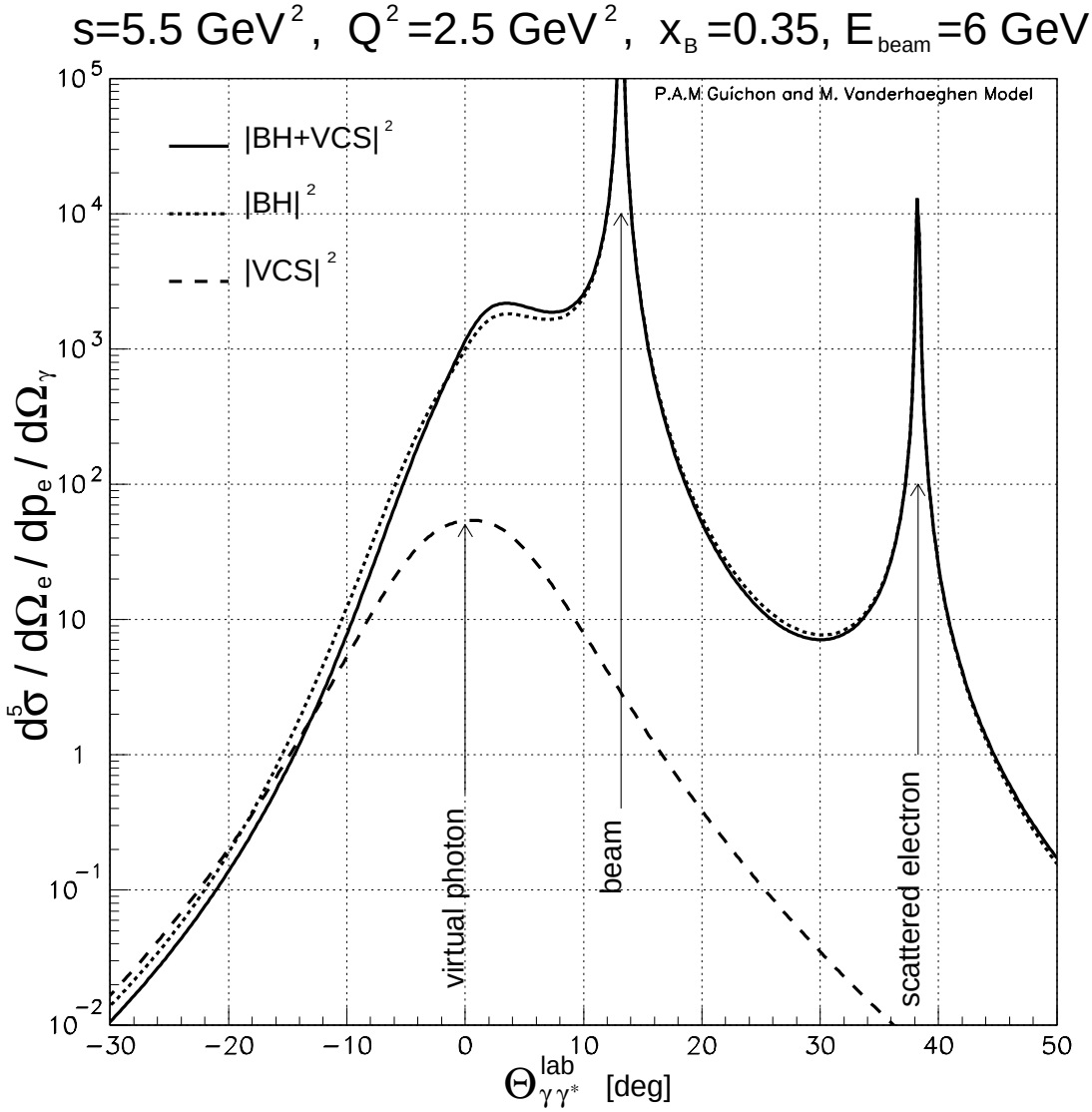

Figure 4: DVCS cross-section (target rest frame) calculated by using a model for the SPD's from P.A.M. Guichon and M. Vanderhaeghen. $\theta^{\rm lab}_{\gamma\gamma^*}$ is the laboratory polar angle between the final photon q' and the VCS virtual photon $q = k - k'$.

The $ep \to ep\gamma$ cross-section is given by:

$$\frac{d^5\sigma^{lp\to lp\gamma}}{dQ^2 dx_B dt d\varphi} = \frac{\alpha_{em}^3}{8\pi}\frac{1}{4x_B M_p^2 E_{lab}^2}\frac{1}{\sqrt{1+4x_B^2 M_p^2/Q^2}}\left|\mathcal{T}_{BH}+\mathcal{T}_{VCS}\right|^2 \tag{1}$$

where $\mathcal{T}_{VCS}$ and $\mathcal{T}_{BH}$ are the amplitudes for the VCS and Bethe-Heitler processes, x_B is the Bjorken variable, φ is the angle between the hadronic and the leptonic planes, t is the transfer between the initial and final state proton defined by $t = (p' - p)^2$.

As we can see from Fig. 4, the Bethe-Heitler dominates the cross-section in energies accessible at Jefferson Lab. It would be very difficult to separate the DVCS cross-section from the Bethe-Heitler. However, as discussed in the previous section, we can benefit from the situation if we consider the difference in cross-section for electrons of opposite helicities. There is no contribution coming from the $|BH|^2$ term. This term, being purely real does not contribute because of symmetry reasons [10]. In our kinematics, the $|DVCS|^2$ contribution is strongly suppressed and the term dominating this cross-section difference is the interference between the BH and the DVCS.

We will effectively use this interference with the BH as a filter and a magnifier. Indeed, it projects out the imaginary part of the DVCS amplitude and also enhances it with the full magnitude of the BH.

3.2 DVCS asymmetry

If we use a longitudinally polarized electron beam, the difference in cross-section for electrons of opposite helicities will have an azimuthal angle (φ) dependence.

We denote by $\mathcal{M}^{\lambda',\lambda}_{\mu',\mu}$ the $\gamma^* p \to \gamma p$ transition amplitude, where $\lambda(\lambda')$ is the helicity of the incoming(outgoing) photon and $\mu(\mu')$ the helicity of the incoming(outgoing) proton.

The different helicity amplitudes of $\gamma^* p \to \gamma p$ play different roles depending on the helicity transfer for the photon:

- The leading twist amplitudes are the $\mathcal{M}^{1,1}_{\mu',\mu}$ amplitudes. They correspond to the handbag dominance and mainly show up in a $\sin\varphi$ dependence on the cross-section.
- The amplitudes $\mathcal{M}^{1,0}_{\mu',\mu}$ involving a longitudinal γ^* are non-leading twist, *i.e.* suppressed by a power of $1/Q$.They predominantly lead to a $\sin 2\varphi$ dependence.
- At leading twist there are $\mathcal{M}^{1,-1}_{\mu',\mu}$ amplitudes. They involve hard scattering of order α_s and gluon SPD's instead of quark ones. With quark exchange these amplitudes are again non-leading twist. The $\mathcal{M}^{1,-1}_{\mu',\mu}$ gives contribution both to the $\sin\varphi$ and $\sin 2\varphi$ terms in the cross-section, but with small coefficients. Note also that in our kinematics, gluon SPD's are expected to be negligible.

The full expression for the difference in the cross-section for leptons of opposite helicities is then given by (2):

$$\frac{d^5\ \overrightarrow{\sigma}}{dQ^2 dx_B dt d\varphi} - \frac{d^5\ \overleftarrow{\sigma}}{dQ^2 dx_B dt d\varphi} = \frac{A\sin\varphi + B\sin 2\varphi + C\sin 3\varphi}{-s'u'} \tag{2}$$

The denominator $s'u' = -4(k\cdot q')(k'\cdot q')$ originates from the electron propagators of the BH process and is completely calculable. Having removed the BH φ-dependence in the cross-section, we will be left with a simple structure in $\sin\varphi$, $\sin 2\varphi$ and $\sin 3\varphi$. Appendix C gives more details about helicity amplitudes.

4 Experimental Goals

The goal of this experiment will be to provide the first checks of the Q^2-dependent scaling of the DVCS amplitude, as well as to evaluate the size of the SPD's (in the A coefficient) and study the higher-twist effects (in the B coefficient).

In order to do so we will measure the out-of-plane angular dependence of the difference in the cross-sections between longitudinally polarized electrons of opposite helicities. This will allow us to access the coefficients A and B of the $\sin\varphi$ and $\sin 2\varphi$ terms. The C coefficient in front of the $\sin 3\varphi$ is negligible as it involves even higher order terms.

Our measurements at several Q^2 values will allow us to study the Q^2 dependence of each of these terms.

Factorization predicts a $1/Q$ behavior of the A coefficient and a $1/Q^2$ behavior of the B coefficient (Eq. 2). These are independent tests of factorization. The A coefficient provides a direct measure of a linear combination of SPD's at $x = \xi$. The determination of the $\sin n\varphi$ coefficients will yield a measurement of the imaginary parts of the proton helicity averaged amplitudes $\widetilde{M}^{1,1}$ and $\widetilde{M}^{1,0}$ weighted by the BH factors, as shown in appendix C.

We will perform three measurements at fixed $x_B \approx 0.35$, with Q^2 ranging from 1.5 to 2.5 GeV^2 in order to study the Q^2 dependence of these amplitudes.

5 Kinematics

We plan to measure the helicity dependent cross-sections for three kinematics using a 6 GeV beam, ranging from Q^2=1.5 to 2.5 GeV^2 at fixed $x_B \approx 0.35$, with s ranging from 3.5 to 5.5 GeV^2. Table 1 summarizes the kinematics.

The choice of the kinematics was governed by a number of considerations:

- Measurement over a wide enough range in Q^2 to test the scaling,
- keep x_B fixed (in a region where quark SPD's should dominate),
- obey certain experimental constraints such as detector position and background considerations.

s GeV^2	Q^2 GeV^2	$-t$ range GeV^2	θ_e deg	$\theta_{\gamma*}$ deg	P_e GeV	P_p GeV/c
5.5	2.5	0.15/0.45	25.1	-13.2	2.2	0.40/0.65
4.5	2.0	0.15/0.30	19.2	-17.3	3.0	0.40/0.60
3.5	1.5	0.15/0.30	14.7	-22.6	3.8	0.40/0.60

Table 1: Proposed kinematics. $\theta_{\gamma*}$ is the angle between the virtual photon and the beam, θ_e is the scattered electron angle, P_e and P_p are the momenta of the scattered electron and recoil proton. The values for t and P_p are the mininum and maximum values for a single kinematic setting, as defined by the angular acceptances of the photon calorimeter and proton detector.

6 Monte-Carlo Simulation

We have performed a Monte-Carlo simulation of the experiment using models of the SPD's from [18]. The simulation takes into account the realistic acceptance of the apparatus and its resolution as well as energy loss and radiative corrections. The yield of events passing the analysis cuts for the main physics quantities is shown in Fig. 5.

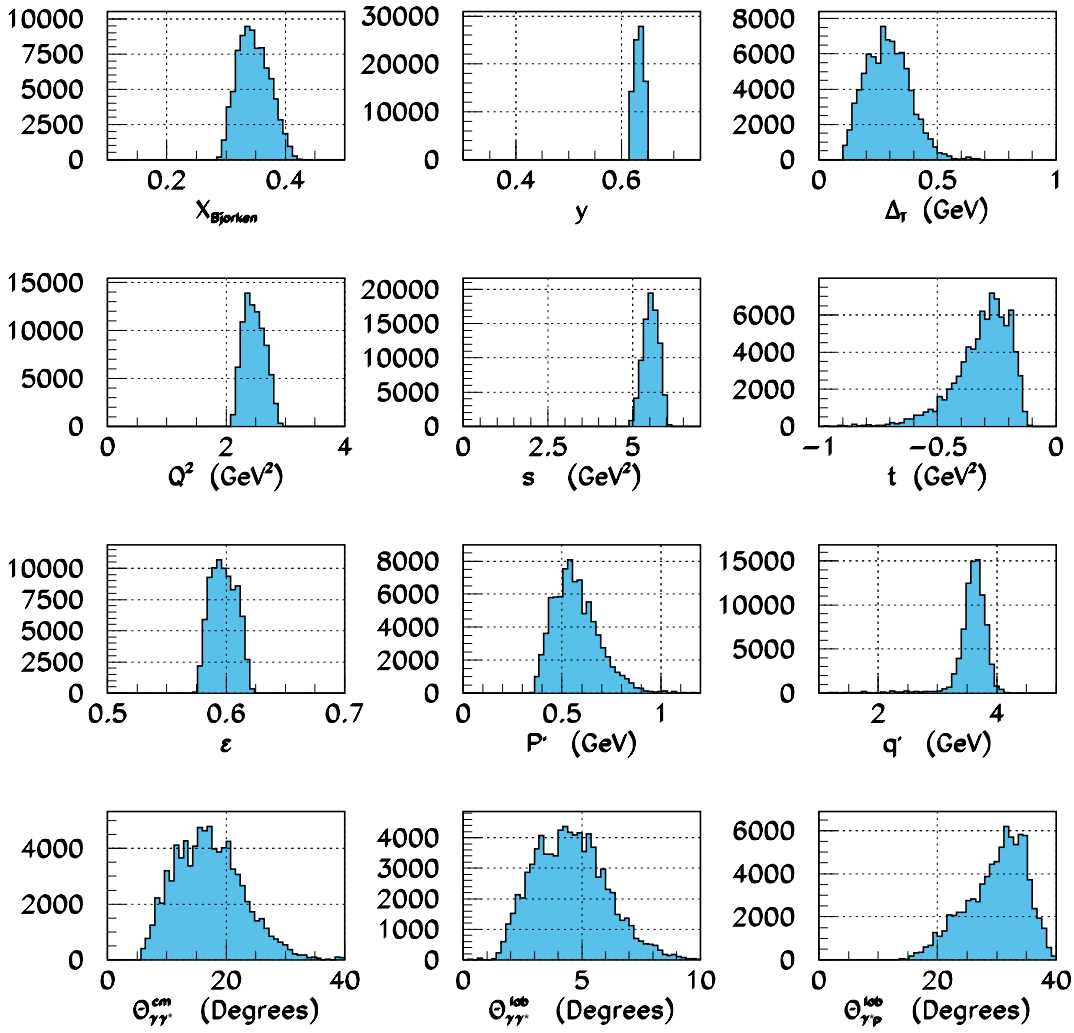

Figure 5: Histograms of main physics variables after all analysis cuts for the kinematical point s=5.5 GeV^2, Q^2=2.5 GeV^2. $x_{\rm Bjorken} \equiv x_B = Q^2/(2M_p\nu)$; $y = \nu/k$; Δ_T = component of $\vec{p}\,' - \vec{p}$ transverse to $(\vec{p}\,' + \vec{p})/2$; $Q^2 = -q^2 = (k - k')^2$; $s = (q + p)^2$; $t = (q - q')^2$; $\epsilon = 1/[1 + 2(\vec{q}^{\,2}/Q^2)\tan^2(\theta_e/2)]$ = virtual photon polarization; p' = recoil proton laboratory momentum; q' = final photon laboratory energy; $\theta^{\rm cm}_{\gamma\gamma^*}$ = angle between final photon and $\vec{q}$ direction in CM frame of final photon and proton; $\theta^{\rm lab}_{\gamma\gamma^*}$ = angle between final photon and $\vec{q}$ direction in lab frame; $\theta^{\rm lab}_{\gamma' p}$ = angle between final proton and $\vec{q}$ direction in lab frame.

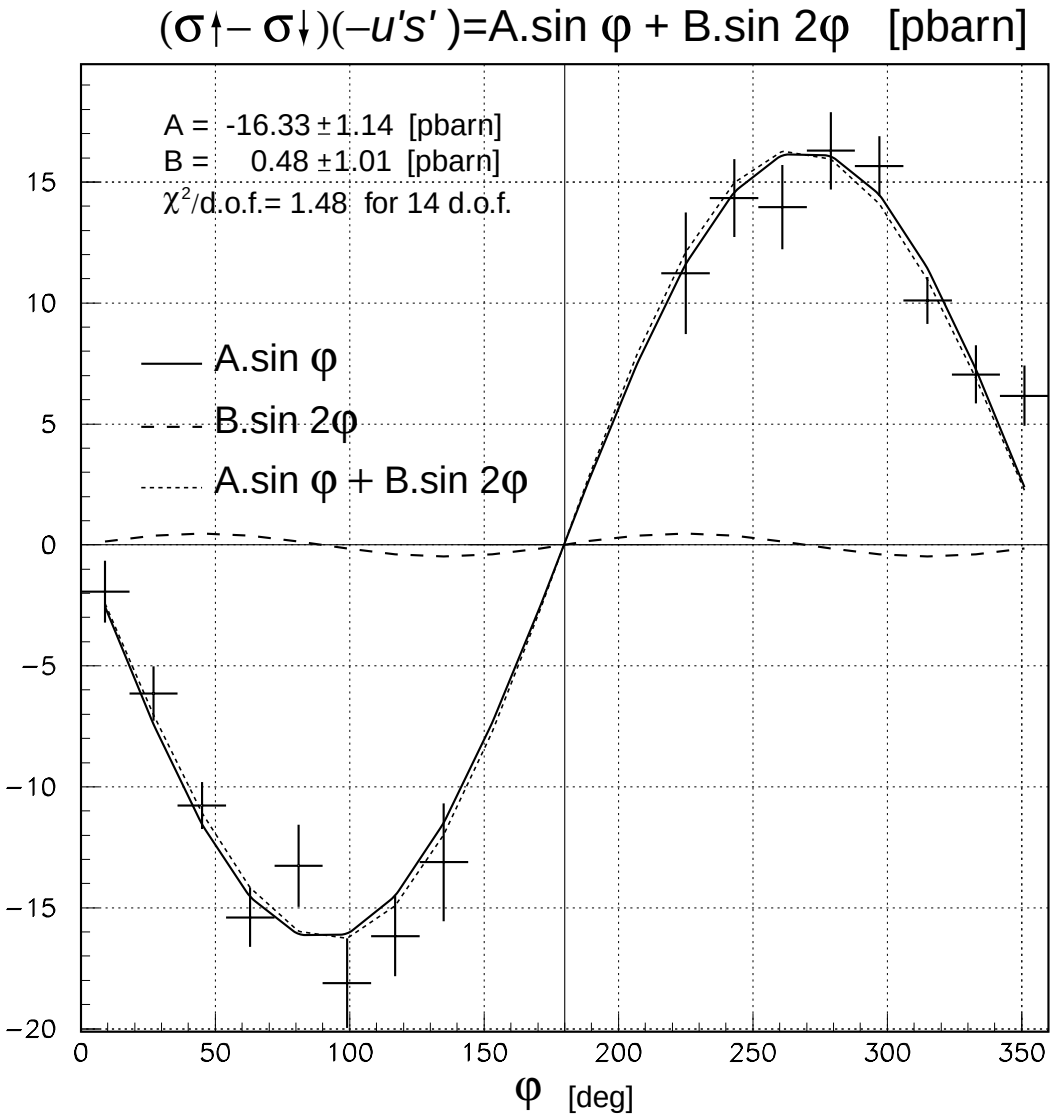

Figure 6: Expected cross-section difference and extraction of A and B coefficients for 200 hours of beam time with a luminosity of 10^{37} $cm^{-2}s^{-1}$ and a beam polarization of 70 %. This is for s=5.5 GeV^2, Q^2=2.5 GeV^2. The model used for the SPD's in the A coefficient is from [18], the model value for B is set to 0. The simulation indicates we can achieve a 8% precision on the SPD (A term) determination and a precision of ±0.06 on the higher twist to leading twist ratio (B/A) determination.

Figure 6 shows the expected difference in the cross sections $\frac{d^5\sigma}{d\Omega_e d\Omega_\gamma dP_e}$ multiplied by the Bethe-Heitler denominator $s'u'$. This was calculated for a beam polarization of 70 % and 200 hours of beam time at a luminosity of $10^{37}\ cm^{-2}s^{-1}$.

The errors bars on the data points represent the expected statistical errors. The curves are a fit of the $\sin\varphi$ and $\sin 2\varphi$ components to show the extraction of the A and B coefficients. It must be noted that in the SPD model we used, there is no $\sin 2\varphi$ term. Therefore, B should be zero which is consistent with the extracted values within error bars.

The statistical accuracy we expect for the A and B coefficients is given in the table below:

s, Q^2	x_B range	$-t$ range	$\frac{\Delta A}{A+B}$	$\frac{\Delta B}{A+B}$
5.5 GeV^2, 2.5 GeV^2	0.30-0.40	0.15-0.45 GeV^2	8.4 %	8.4 %
4.5 GeV^2, 2.0 GeV^2	0.30-0.45	0.15-0.30 GeV^2	8.0 %	6.0 %
3.5 GeV^2, 1.5 GeV^2	0.30-0.45	0.15-0.30 GeV^2	8.0 %	6.0 %

Table 2: Relative statistical accuracy expected on the determination of A and B coefficients. We have assumed a beam polarisation of 70% and 200 hours of data taking for each kinematics with a 10^{37} $cm^{-2}s^{-1}$ luminosity.

7 Experimental setup

We will use a longitudinally polarized electron beam, along with the 15 cm Hall A hydrogen cryotarget. The Hall A electron spectrometer will be used to detect the scattered electrons. The recoil proton will be detected in a ring of segmented plastic scintillators (see section 7.2). The emitted photon will be detected in an electromagnetic calorimeter (see section 7.3). A schematic of the experimental setup is shown in Fig. 7.

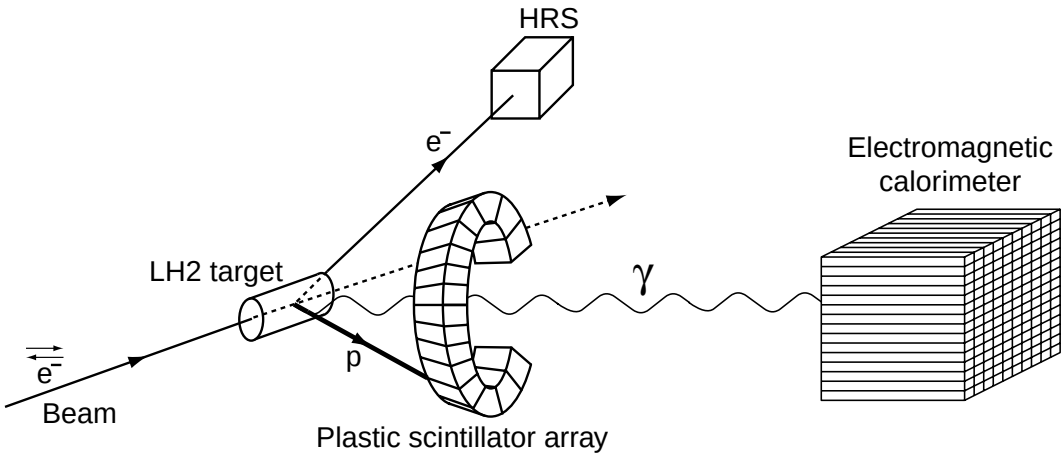

Figure 7: Schematic of the proposed experimental setup for DVCS.

7.1 Modifications to the vacuum target chamber

The present target chamber has 1" thick aluminum walls and no windows for recoil protons. We plan to have a special target chamber, with a window for the electron arm spectrometer and another one for the photon and recoil proton. The recoil proton can have a momentum as low as 400 MeV/c,

corresponding to a range of 2.49 cm in aluminum. We will shield the scintillators by using an aluminum window of less than 1 cm thickness on the vacuum chamber.

7.2 The proton detector

As shown by the background studies (section 8), we need to detect the recoil proton to perform coplanarity cuts. As illustrated in Fig. 8, even a small angular acceptance for q' around the $\vec{q}$ direction requires a large angular acceptance for the recoil proton.

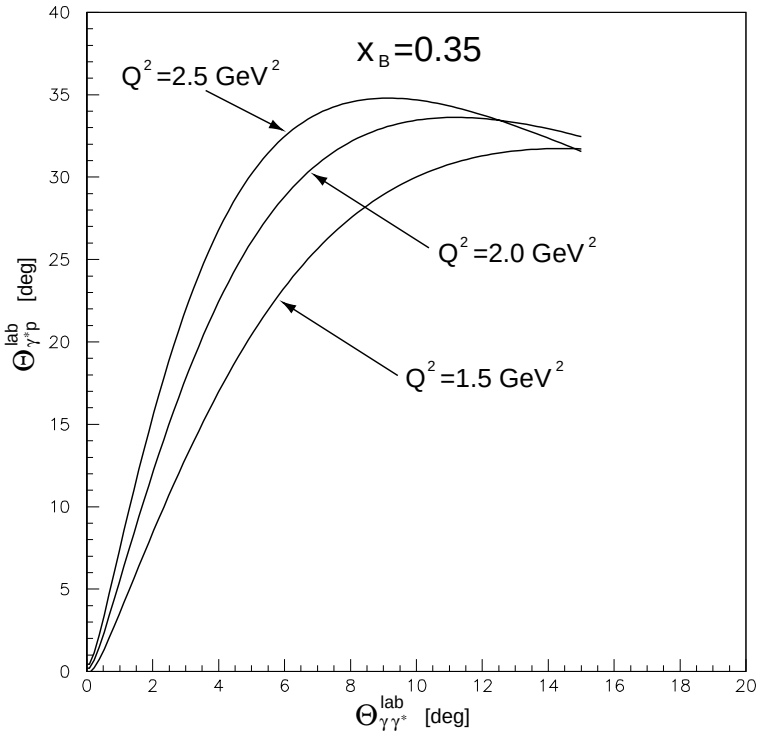

Figure 8: Relation between $\theta_{\gamma\gamma^*}$ (angle between the emitted photon and the virtual photon) and $\theta_{\gamma^* p}$ (angle between the virtual photon and the recoil proton) in the laboratory frame. The experimental acceptance is illustrated in Fig. 5.

The hadron spectrometer cannot be used since the recoil protons are highly out-of-plane. Therefore, we propose building a segmented ring of scintillators to cover the range of φ from 45° to 315° and provide good angular resolution for acoplanarity tests. This ring has to be located close to the target to keep it to a manageable size and to minimize consequences of multi-scattering on the target chamber. We plan to place it about 60 cm from the target.

The singles counting rate in the scintillators will be high due to various target related backgrounds. We will equip the photomultipliers with a fast ADC sampling system, the same one that will be used for the calorimeter in order to manage high counting rates.

We will shield the proton detector from low energy particles (with one centimeter of aluminum) without losing much in the proton detection efficiency.

The proton detector shown in Fig. 7 is a ring of plastic scintillators located around the direction of the virtual photon. The ring is partially open in the forward direction (between -45° and +45°) to let the beam and the real photon through. The angle between the scattered proton direction and the average of the virtual photon direction in the laboratory frame will cover a range of $18° < \theta_{\gamma^* p} < 38°$. This corresponds to a coverage of $1° < \theta_{\gamma\gamma^*} < 10°$ (Fig. 5). We plan to segment the proton detector

in φ (as shown in Fig. 7) and θ (not shown). The segmentation is driven by resolution and singles rates considerations and is discussed in Section 10.3.

One must note that once we have all the information on the scattered electron and real photon, we can restrict the analysis of the proton detector to where we expect the proton to hit the detector (maybe 3 or 4 scintillator segments maximum). That way, we are not sensitive to the rate in the whole detector for the analysis of the $ep \to ep\gamma$ events.

7.3 Photon calorimeter

The scattered photon will be measured by an electromagnetic calorimeter, currently under construction by the RCS collaboration [24]. The calorimeter consists of 704 blocks of TF-1 lead glass, arranged in an array of 22 columns by 32 rows. Each block is 40 cm long and 4x4 cm^2, leading to a total size for the calorimeter of about 0.9 m wide by 1.3 m high. The calorimeter will be centered at the nominal angle θ_{γ^*} of the virtual photon (Table 1) and placed 4 m from the target. We plan to instrument the calorimeter with a fast ADC sampling system so we can manage the anticipated large amount of pile-up. Also, we will shield it from the low-energy electromagnetic background as well as the hadronic background using a one inch layer of aluminum in front.

7.4 The fast ADC sampling

Since the calorimeter is in direct view of the target and rather close to the beam pipe, we expect a high counting rate in it. This induces pile-up and limits the luminosity. Solving this pile-up problem will allow us to reach a higher luminosity and perform the experiment in a reasonable time scale.

The usual technique of using a narrow gate (40 ns) ADC after the phototube can not deal with more than a few percent of pile-up. Moreover, the energy and spatial resolutions are degraded significantly. The solution is to sample the signal, in order to perform a shape analysis and subtract the pile-up events from the DVCS events. This technique was already used successfully in a somewhat crude way in the SLAC E154 and E155 experiments using three TDC levels [25].

We propose doing a shape analysis of each calorimeter channel over 256 ns. The device will work with pretrigger at a rate of 1 GHz and will be able to acquire events after coincidence with the HRSe spectrometer at a rate of 1 kHz [26]. More details about the fast ADC sampling system can be found in appendix D.

We plan to equip our ring of proton scintillators with the same sampling device, using a slightly different version of the pretrigger.

8 Competing channels

There are two principal competing channels to the DVCS process: (i) π^0 electroproduction (Fig. 9d); (ii) pion associated production at the photon electroproduction (Fig. 9e,f,g).

In order to select VCS events one must make sure that we select photon electroproduction events. We have two techniques:

- missing mass cut in $H(e, e'\gamma)X$,
- acoplanarity cut (virtual photon, recoil proton and emitted photon required on plane).

We need to determine:

- the scattered electron four-momentum. Along with the knowledge of the beam energy, fixes the four-momentum of the virtual photon,
- the recoil proton direction and the emitted real photon four-momentum.

We will measure the direction and energy of the emitted photon and the direction of the recoil proton. It must be noted, that this relaxes the requirements on the missing mass resolution in constrast with the VCS case where one only detects the recoil proton. It is indeed easier to separate M_p^2 from $(M_p + M_\pi)^2$ (photon energy and direction measured, missing mass on the proton) than 0 from M_π^2 (proton energy and direction measured, missing mass on the photon). There is a factor of twenty between the required resolutions on the missing mass squared. In addition, we will require coplanarity conditions on the virtual photon, the recoil proton and the emitted photon.

Figure 10 shows the missing mass spectrum in $H(e, e'\gamma)X$. One must note that the proton information is not used at this time. Figure 11 shows the acoplanarity parameter (using the proton direction information) for various processes with and without a missing mass cut. The acoplanarity parameter is define as follows:

$$Aco = \arccos\left(\frac{q' \times q}{|q' \times q|} \cdot \frac{q' \times p}{|q' \times p|}\right) \tag{3}$$

The $ep \to ep\gamma$ are clearly isolated after both cuts. The contamination from associated events and π^0 electroproduction is less than 1%.

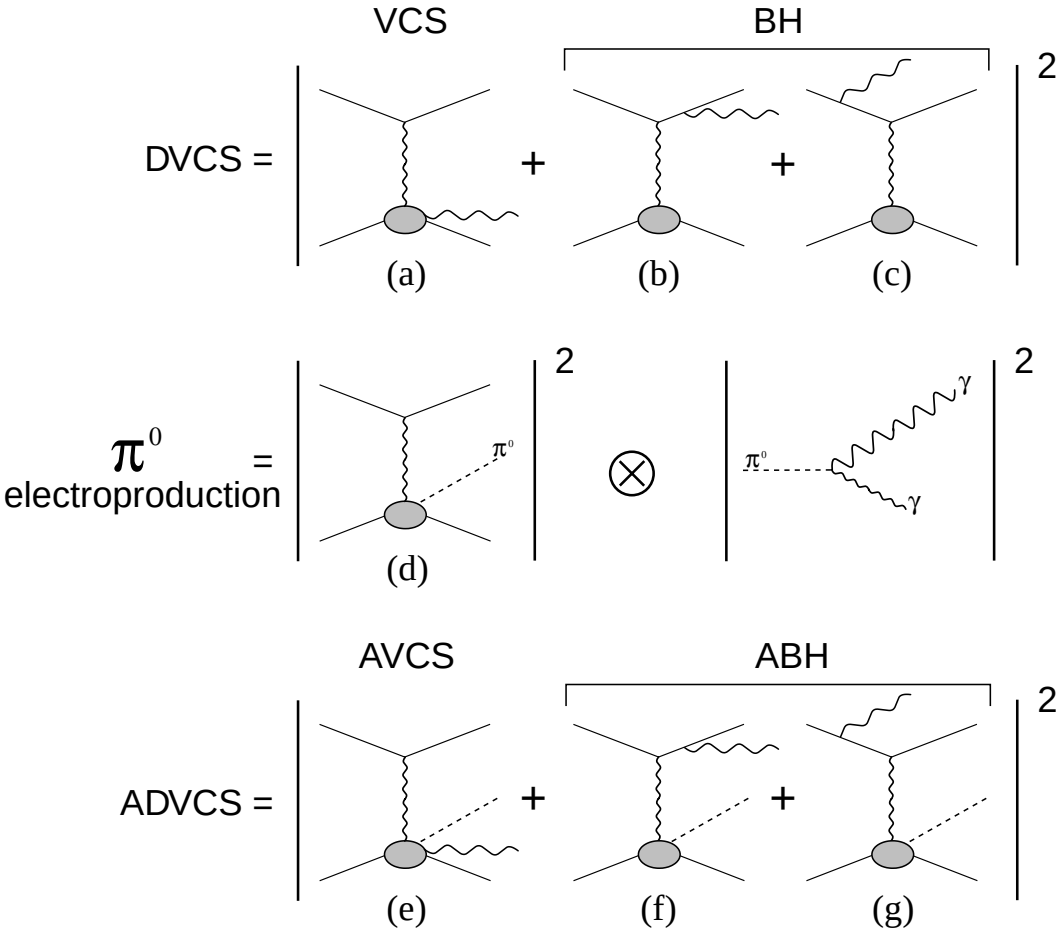

Figure 9: Lowest order diagrams of electroproduction of photon, pion, or photon plus pion. Top: VCS and BH amplitudes. Middle: π^0 electroproduction which contributes to a background $ep \to ep\gamma\gamma$. Bottom, Associated production: $ep \to e\gamma(\Delta \text{ or } N^*)$ (Δ or $N^* \to N\pi$).

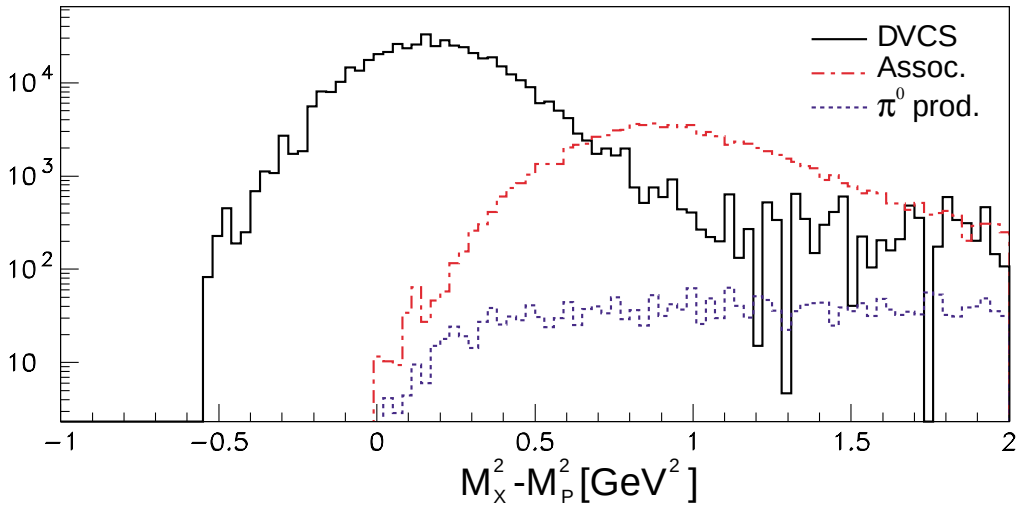

Figure 10: Missing mass spectrum for different processes. The horizontal axis represents the missing mass $M_X^2 - M_p^2$ in units of GeV^2, the vertical axis is the number of events for 200 hours of beam time at a 10^{37} cm^{-2}s^{-1} luminosity. The solid curve is the DVCS, the dot-dashed curve is the Δ or N^* production, the dotted curve is the π^0 production. The figure corresponds to the case where one detects the scattered electron and the emitted DVCS photon (the proton is not detected).

8.1 π^0 electroproduction

The π^0 electroproduction diagram is shown on Fig. 9d.

When the π^0 decays with a photon emitted in the forward direction, the second photon from the π^0 is backward and has a very low energy (a few MeV). The final products of this reaction are exactly the same as for VCS except for a very difficult to detect soft backward photon. The missing mass and coplanarity techniques can not discriminate between these two types of events. The solution is to select symmetric π^0 decay events for which we detect both photons in the calorimeter. Using these events we can extrapolate the π^0 background and subtract its contribution from the events with only one photon recorded.

In the DVCS kinematics:

- The π^0 production cross-section decreases $1/Q^2$ faster than the DVCS [18],
- no interference enhances the cross-section, in contrast to the DVCS which is amplified by the BH when the transfer t is small. Therefore, the π^0 cross-section is actually smaller than the interference between the DVCS and BH processes,
- theorists expect the beam helicity asymmetry to be very small.

We note that the π^0 cross section is in itself a very interesting measurement. In the DVCS kinematics, it is sensitive to another combination of SPD's [18].

8.2 Associated pion production

Another parasitic reaction is associated pion production with photon electroproduction: this is the DVCS or BH production of an N^*. The corresponding diagrams are shown in Fig. 9e,f,g. There are two different channels:

$$\begin{array}{rl} ep \rightarrow & e\gamma \ \Delta, N^* \quad (a) \\ & \hookrightarrow \ \pi^+ n \end{array}$$

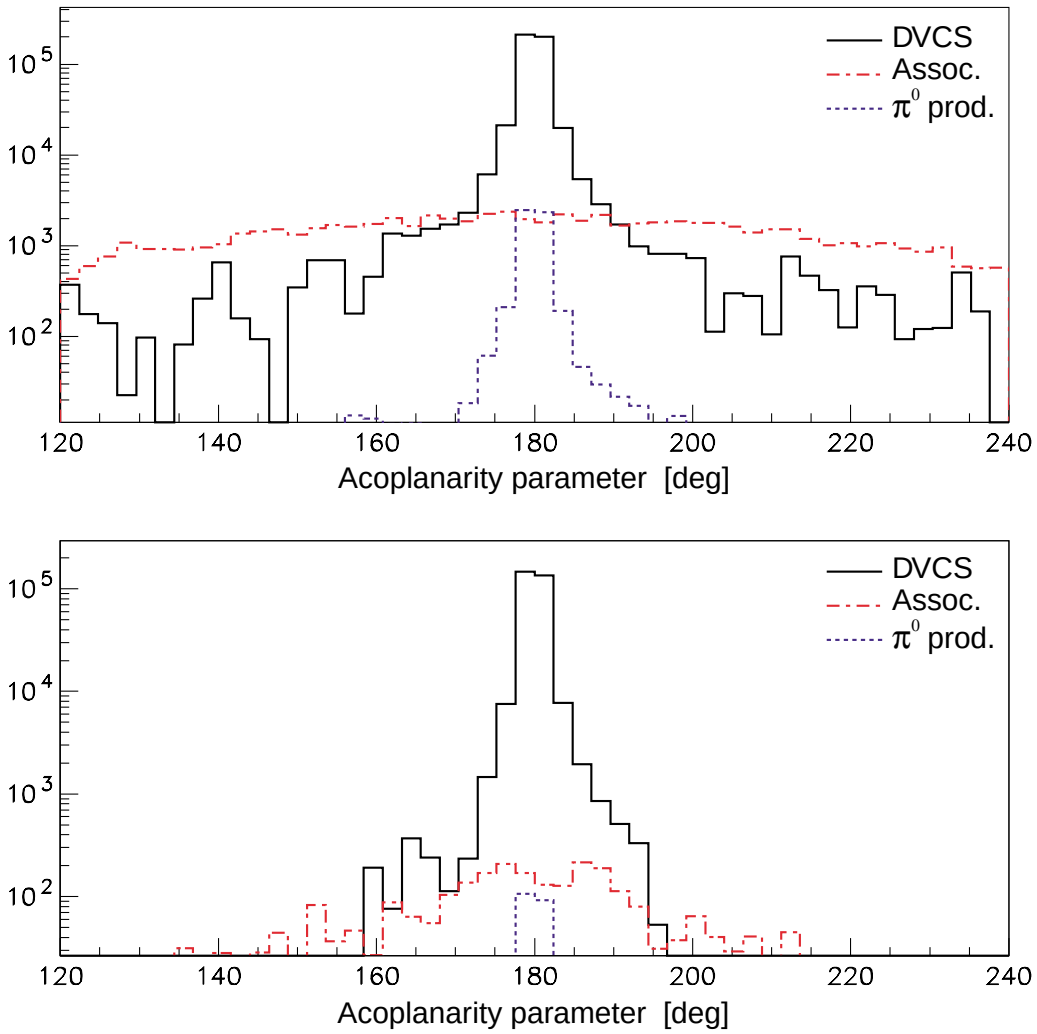

Figure 11: Acoplanarity parameter (as defined in Eq. 3) for DVCS (solid curve), Δ or N^* production (dot-dashed curve) and π^0 production (dotted curve). The horizontal axis represents the acoplanarity angle in degrees, the vertical axis is the number of events for 200 hours of beam time and a luminosity of 10^{37}. The top figure is without cuts, the bottom figure has a missing mass cut $-0.5 < M_X^2 - M_p^2 < 0.5$ GeV^2.

and

$$ep \to e\gamma \begin{array}{l} \Delta, N^* \quad (b) \\ \hookrightarrow \pi^0 p \end{array}$$

The diagrams of Fig. 9f,g are the associated pion production via the BH process (ABH). These diagrams (f,g) require the knowledge of the pN^* or $p\Delta$ transition form factors to be interpreted.

The diagram in Fig. 9e is the associated pion production via the DVCS process (AVCS). This is the DVCS production of a Δ or N^*. Diagrams (e) (f) and (g) lead to the same final state and therefore all three interfere.

The physics of diagram (e) is just as important as the physics of the DVCS process. Indeed at high enough mass of the pion-nucleon system (*i.e.* Δ or N^*), AVCS gives access to some of the transition SPD's. However, extracting the AVCS amplitude is more complicated in that case since ABH is no longer purely real but has an imaginary part as well (due to the extra emitted pion).

Close to the pion threshold ($\pi - N$ system in s-wave), we expect that a low energy theorem (LET) can be used to connect the AVCS and exclusive DVCS amplitudes. The same idea predicts that $ep \to e\gamma\pi^0 p$ is much smaller than $ep \to e\gamma\pi^+ n$. This is a consequence of the Adler consistency rule: the first order term in the LET expansion vanishes in the π^0 case.

Detecting the recoil proton will suppress the $n\pi^+$ channel. We consider a $\Delta E - E$ segmentation of the proton detector to veto neutrons.

It has been estimated [27] that the $\Delta(1232)$ cross-section ($ep \to e\Delta\gamma$) is an order of magnitude smaller than the DVCS in our kinematics. Moreover the asymmetry is predicted to be small, *i.e.* $\sim 7\%$ whereas the DVCS asymmetry is of the order of 30%.

Figure 12 represents the asymmetry (left) and the cross-section for the associated pion production (dashed line) and the DVCS (solid line). The curves are drawn for various angles of $\theta_{\gamma\gamma^*}$ [28].

9 Electromagnetic background

In our kinematics, the ring of scintillators subtends a large solid angle ($\Delta\theta \otimes \Delta\phi = 20^\circ \otimes 270^\circ$) and is placed close to the target (about 60 cm). This choice allows us to match the real photon and recoil proton acceptances. Putting the ring further away would have resulted in a significant increase of the dimensions of this apparatus. This raised the issue of singles rates due to low-energy electromagnetic background coming from the target and the beam pipe. Fortunately, the RCS experiment has similar concerns and was able to perform tests in Hall A. A block of $20 \times 20 \times 20\text{cm}^3$ of scintillator was placed 10 m away from the target at an angle of 29.8°. The lead-glass electromagnetic calorimeter was placed at 42°. The results are presented in [29]. Although these tests are not an exact match of our kinematics or luminosity, they do show that it is possible to control the electromagnetic noise at a level compatible with our experiment.

10 Systematic errors

10.1 Beam polarization

If the beam polarization has an additional transverse component, it will not generate any asymmetry since the transverse asymmetries are suppressed by a factor m_e/E_e. We would just have a dilution factor that would enter linearly in the errors in the determination of A and B. However, it must be noted that the ratio B/A is independent of the error on the beam polarization. In the DVCS regime the B/A ratio is expected to go to zero with a $1/Q$ dependence.

10.2 Luminosity

This is given by the knowledge of the beam current and the target density. The luminosity can be cross-calibrated with a number of known processes:

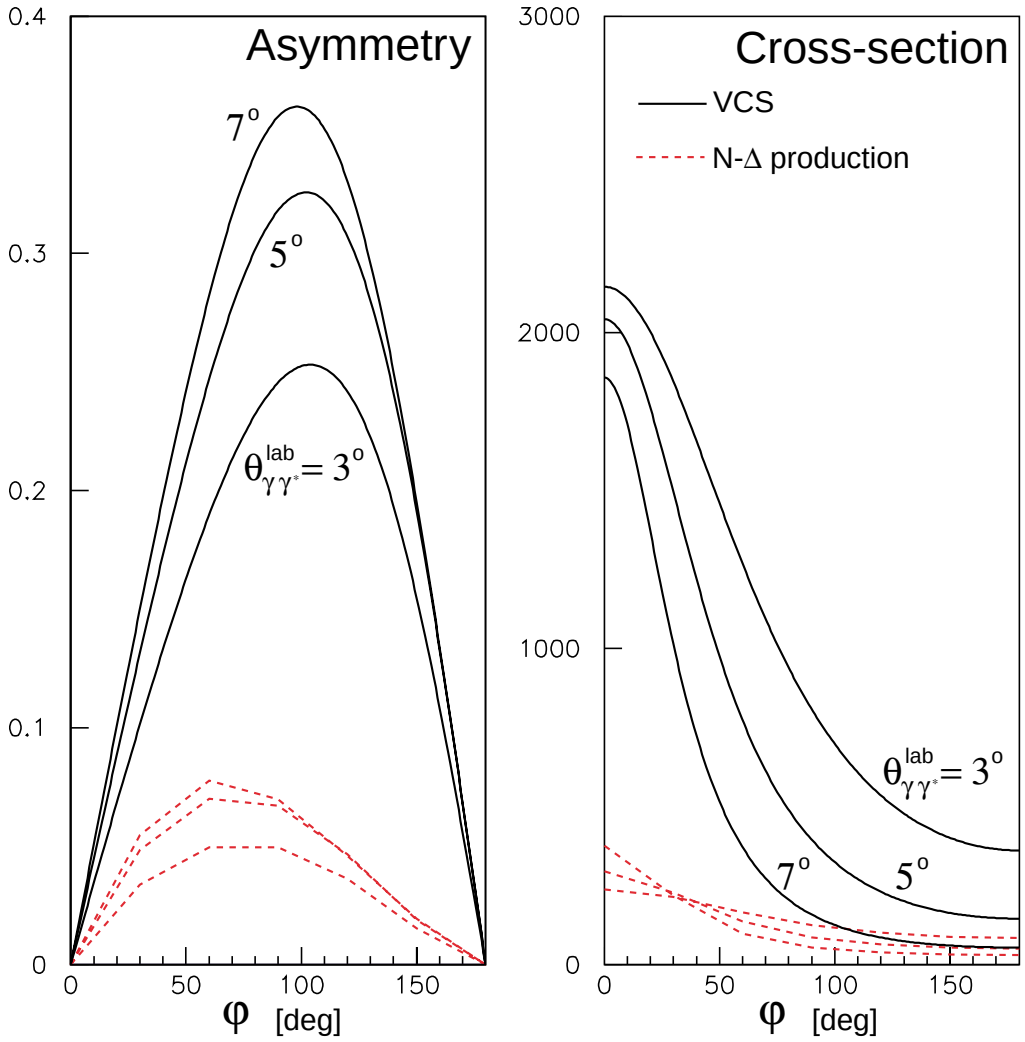

Figure 12: Asymmetry (left) and cross-section (right) for the VCS (solid line) and the Δ or N^* production (dashed line) at s=5.5 GeV^2, Q^2=2.5 GeV^2. For both VCS and resonance production asymmetries, the curves correspond to $\theta_{\gamma\gamma^*}$=3, 5, 7° from bottom to top. For the cross-sections, the curves correspond to $\theta_{\gamma\gamma^*}$=3, 5, 7° from top to bottom at $\varphi = 180°$.

- The sum $d\sigma^{\rightarrow} + d\sigma^{\leftarrow}$ is the unpolarized cross-section and is dominated by Bethe-Heitler. This will be used to cross-check the relative normalization between different parts of the data taking.
- The singles counting rate in the electron spectrometer is the inclusive deep inelastic cross-section. This has been well studied by other experiments.
- Here also, the ratio B/A is not sensitive to errors in luminosity.

10.3 Angular resolution of the calorimeter

The angular determination of the scattered photon will require knowledge of the following:

- The scattered electron in the HRSe, which fixes the direction of the virtual photon.
- Vertical vertex position accuracy of the order of 0.5 mm. The accuracy of the beam position monitors is currently of the order 0.1 mm.
- Horizontal vertex position accuracy which is $\approx \sigma(y_{\rm tg}^{\rm HRS})/\sin\theta_e^{(0)}$, where $\sigma(y_{\rm tg}^{\rm HRS}) \approx 1$ mm is the precision of the horizontal coordinate of the electron track at the target. This vertex precision contributes as follows to the determination of the horizontal angle of the detected photon: $\sigma_{\theta_\gamma} = \sigma(y_{\rm tg}^{\rm HRS})\sin\theta_\gamma/[L_{cal}\sin\theta_e]$, where L_{cal} is the distance between the target and the calorimeter.
- Calorimeter spatial resolution of 5 mm. This has been achieved and is sufficient to contribute only 1.25 mr to the accuracy on the real photon direction. This is approximately equal to the contribution from the vertex resolution.

In table 3 we list for each kinematics the various systematic contributions and the resulting uncertainty in the angle $\theta_{\gamma\gamma*}$ in the laboratory frame.

s Q^2	$(\mathrm{HRS}_e\&\mathrm{Target})_{hor.}$	$(\mathrm{HRS}_e)_{vert.}$	Calo.	$\Delta\theta_{\gamma\gamma^*}$
5.5 GeV^2, 2.5 GeV^2	1.2 mr	1 mr	1.25 mr	0.135°
4.5 GeV^2, 2.0 GeV^2	1.3 mr	1 mr	1.25 mr	0.241°
3.5 GeV^2, 1.5 GeV^2	1.3 mr	1 mr	1.25 mr	0.241°

Table 3: we have taken an angular resolution of 1 mr, and a transverse resolution of 1 mr for the HRS, a spatial resolution of 5 mm for the calorimeter located at 4 m from the target.

Good angular resolution will give us an extra handle on the associated production rejection. The jacobian $\frac{d\theta_{\gamma^* p}}{d\theta_{\gamma\gamma^*}}$ is large (~ 10) in the relevant $\theta_{\gamma\gamma^*}$ range. Figure 8 gives the relation between the angles $\theta_{\gamma\gamma^*}$ and $\theta_{\gamma^* p}$.

An azimuthal segmentation of 100 mr for the proton detector gives a good match to the precision of the direction of the proton as predicted by the electron and emitted photon measurements. Together with a segmentation of 100 mr in the proton polar angle, this corresponds to a total of approximately 150 scintillator elements.

10.4 Radiative corrections

Our simulation took the external radiative corrections into account by radiating photons on the electron lines. We believe that for this experiment, the effect of internal radiative corrections (*i.e.* radiating an additional real photon) is comparable to elastic scattering or other exclusive processes (in this case the radiative corrections are much smaller than *e.g.* low-x_B inclusive processes). The QED radiative corrections have recently been estimated for the DVCS process at Jefferson Lab kinematics [30]. The authors show that these corrections are up to 25% on the cross-section but are rather small on the asymmetry itself (of the order 5%).

11 Estimation of counting rates and accidentals

Counting rates in the calorimeter were estimated using P. Degtiarenko's Monte-Carlo simulation [31]. The counting rates have been found to be a factor 2 smaller than these estimations during the RCS tests in 1998 and 1999. This calculation therefore gives a "reasonable" over-estimate. The singles rate in the calorimeter is mostly due to photons and is rather high (of the order of a few MHz) if the energy threshold is 500 MeV (*cf.* tables 4 and 5). However, one can set a very specific cut (by software) on the measured photon energy in the calorimeter (E_γ) which lowers this rate by a factor R, as large as ~ 30 for the highest Q^2 kinematics. R is the ratio of the events for which $E_\gamma > 500$ MeV to the events for which $0.9p_\gamma < E_\gamma < 1.1p_\gamma$ ($\pm 10\%$ variation around the nominal emitted photon energy, which contains almost all the $ep \to ep\gamma$ events, as shown in Fig. 5).

s [GeV^2]	Q^2 [(GeV/c)^2]	θ_γ [deg.]	p_γ [GeV/c]	p_e [GeV/c]	θ_e [deg.]
3.5	1.5	-22.6	2.1	3.8	14.7
4.5	2.0	-17.3	2.9	3.0	19.2
5.5	2.5	-13.2	3.7	2.2	25.1

Table 4: Summary of kinematic variables for the three settings. p_γ is the nominal momentum of the emitted photons in the $ep \to ep\gamma$ reaction. The distribution of the photon energy spreads around $\pm 10\%$ of this value.

$N_\gamma^{>500MeV}$ [s^{-1}]	R	$N_\gamma \cdot \tau$	$N_\gamma \cdot \tau / R$	σ_{DIS} [nb·GeV^{-1}sr^{-1}]	$N_{DIS}^{e^-}$ [s^{-1}]	Accid. [s^{-1}]	$N_{DVCS}^{Mx\,cut}$ [s^{-1}]	Dilution factor
$2.2{\cdot}10^6$	16.3	0.011	$6.7{\cdot}10^{-4}$	74.6	1709	1.15	0.87	0.43
$7.8{\cdot}10^6$	24.2	0.039	$1.6{\cdot}10^{-3}$	20.4	467	0.75	0.58	0.43
$2.2{\cdot}10^7$	32.1	0.11	$3.4{\cdot}10^{-3}$	6.8	156	0.53	0.28	0.39

Table 5: Summary of counting rates in the HRSe, the calorimeter, along with the rates of accidentals and DVCS events. The three lines correspond to the three kinematic settings of table 4. The first column gives the number of photons in the calorimeter with an energy over 500 MeV, as given by P. Degtiarenko's Monte-Carlo. The ratio of the number of photons with $E_\gamma > 500$ MeV to the photons in the DVCS window ($\pm 10\%$ around the nominal photon energy E_γ) is given in the second column by R. The third column gives the occupation of the calorimeter, with a threshold of 500 MeV, for a random $\tau = 5$ ns timing window on the leading edge of pulse. The fourth column gives the occupation once corrected for R. The fifth column gives the DIS cross-section. The sixth column gives the counting rates from DIS in the HRSe. The accidentals rate from the coincidence of the HRSe and the calorimeter is given in column seven. The eigth column gives estimates for the DVCS rates, with a missing mass cut $|M_X^2 - M_p^2| < 0.5$. The last column gives the dilution factor due to the accidentals.

Counting rates in the HRSe were estimated using DIS cross-sections[2]. Indeed, the inefficiency of the electron arm for electrons is of the order of only a few percent. One finds that the rate in the HRSe will be rather low (from 400 Hz at $s = 3.5$ GeV^2, $Q^2 = 1.5$ GeV^2, down to 40 Hz at $s = 5.5$ GeV^2, $Q^2 = 2.5$ GeV^2), as shown in tables 4 and 5.

Assuming a coincidence resolution of about $\tau = 5$ ns, and using the previous results for the rates in the HRSe and the calorimeter, the accidentals rate would be about 1 Hz in the lowest s kinematic setting, whereas the DVCS accounts for 0.87 Hz, the trues over falses ratio is therefore of the order

[2]We have assumed a solid angle of 6.7 msr and a momentum bite of $\pm 4.5\%$ for the HRSe, at a luminosity of 10^{37} cm^{-2}s^{-1}

1. Table 5 gives those estimates for all three kinematic settings. Coincidence between the calorimeter and the electron arm is definitely feasible and the dilution from the accidentals is of the order 0.5. In any case, the subtraction of the accidentals is straightforward and will only lead to an increase of the error bar.

We don't have estimates for the proton detector rates at this time, but the RCS collaboration has performed a test with a shielded scintillator block at a luminosity of 10^{38} cm^{-2}s^{-1} and managed to see clear coincidences with a calorimeter. A test run is planned in the near future to measure counting rates in a scintillator block, in the DVCS conditions. Assuming the rates are of the same order as in the calorimeter (about the same solid angle), we will manage to do triple coincidences and our true to false ratio would be even better by a factor of 10.

This counting rate study shows that one can perform the experiment using a two-arm setup (HRSe and calorimeter). We would already do at least as well as what HERMES can do, but in a much shorter time due to our higher luminosity (see details in next section). The proton detector is however necessary to ensure the exclusivity of the events, resulting in a cleaner interpretation of the data.

12 Comparison with other experiments

The feasability of the DVCS experiment with the CERN 200 GeV muon beam is currently under study. It is proposed to upgrade the experimental COMPASS[32] setup with a recoil detector in order to make the DVCS experiment possible. The latter will cover the kinematical domain $0.05 < x_B < 0.3$ and $2 < Q^2 < 5$ GeV^2. At 200 GeV lepton energy, there is a clear dominance of the DVCS over the BH. The main differences with our experiment are the luminosity (see table 6) and the fact that the CERN experiment measures the squared modulus of the amplitude. It is thus sensitive both to the imaginary part (where the SPD's are evaluated at $x = \xi$, as in our proposed experiment) and to the real part where a convolution over x is involved, which may allow the extraction of the SPD's at $x \neq \xi$.

Among the various processes that allow one to access SPD related observables, the hard exclusive electroproduction of mesons - $\pi^{0,\pm}$, $\rho^{0,\pm}$, ω, ϕ, ... - is also promising. Indeed, a QCD factorization proof has been given recently. In the deep meson case, it is the cross section for absorption of longitudinally polarized photons that factorizes and dominates in the high-Q^2 limit. This is associated with the exchange of a hard gluon.

HERMES has published results in the kinematical range $0.3 < x_B < 0.5$ and $2 < Q^2 < 4$ GeV^2 for the deeply virtual ρ^0_L production [33]. The main limitation of HERMES is luminosity ($\mathcal{L} \approx 10^{32}$ cm^{-2}s^{-1}). To infer the (virtual photon) longitudinal cross-section from the HERMES (and HERA) cross section for electro-production of longitudinally polarized ρ-mesons, one assumes s-channel helicity conservation (SCHC) $d\sigma(e, e'\rho_L) \approx d\Gamma\epsilon d\sigma_L(\gamma^*, \rho_L)$. Because the SCHC hypothesis is tested within $5 \div 10\%$ in the same experiment, this introduces only a small model dependence in the interpretation of the data. The fact that the deep meson process involves the convolution of the SPD with the meson distribution amplitude can be seen as an additional theoretical uncertainty as well as a positive point since not so much is known about the meson wave function.

An approved experiment in Jefferson Lab hall B plans to measure the exclusive electroproduction of the ρ^0 and ω vector mesons in the Bjorken regime $0.1 < x_B < 0.45$ and $1 < Q^2 < 4.5$ GeV^2 [34]. The main feature of the hall B experiment compared with HERMES is 2 orders of magnitude higher luminosity, but lower cross sections (about a factor 4) at the same Q^2 and x_B.

In a totally different kinematical domain, HERA has reported to have seen DVCS events in the region $5 \cdot 10^{-4} < x_B < 10^{-2}$ and $Q^2 > 6$ GeV^2 [35]. Such a small x_B suggests HERA is mostly sensitive to the gluon degrees of freedom whereas measurements at Jefferson Lab, COMPASS or HERMES probe the nucleon in the valence quark region. The exclusivity of the events has been questioned since the recoil proton goes undetected at low angles down the forward beam pipe thus the results may include contributions from inelastic $p(e, e'\gamma)N^*$ processes.

The main features of all those experiments are summarized in table 6, The strong features of the current proposal are that it:

- ensures of the exclusivity of the events (by detecting the proton in triple coincidence with both the photon and the electron),
- achieve high statistical precision ($\mathcal{L} \approx 10^{37}$ cm^{-2}s^{-1}),
- measures a linear combination of the SPD's at the point $x = \xi$, due to the fact that only the interference between the (real) BH and the imaginary part of DVCS enters in the single spin asymetry. In fact, one measures a so-called "envelope" function e.g. $H(x = \xi, \xi, t)$, from which the skewedness (or ξ) effect can be seen by comparison with the known forward parton distributions e.g. $q(x = \xi)$. So, even though the $ep \to ep\gamma$ cross section is dominated by the trivial BH process at CEBAF energy, we can extract from our experiment useful information about the DVCS amplitude.

There is no doubt however, that it is only the first step in the study of the SPD's and more experiments will be necessary. Our proposed experiment is an initial attempt in this direction and will provide an important test of the SPD models available today. A full separation and measurement of the SPD's over the whole x and ξ range will require new facilities. A particularly interesting project would be to use a positron beam. It would give us access to the real part of the DVCS amplitude via charge asymmetry [38].

Experiment	Process(es)	Status	$\mathcal{L}$	Exclus.	x_B	Q^2 [GeV^2]	Observables, comments
HERMES	$ep \to e\rho^0 p$	pub.	10^{32}	No	0.3 - 0.5	2 - 4	$\|\mathcal{A}\|^2$
Hall B	$ep \to e(\rho, \omega)p$	approv.	10^{34}	Yes	0.1 - 0.45	1 - 4.5	$\|\mathcal{A}\|^2$
COMPASS	$\mu p \to \mu(\gamma, \pi)p$	study.	10^{32}	Not yet	0.05 - 0.4	2 - 5	$\|\mathcal{A}\|^2$
HERA	$ep \to e\gamma p$	pub.	10^{30}	No	10^{-4} - 10^{-2}	> 6	gluon sector
Hall A	$ep \to e\gamma p$	prop.	10^{37}	Yes	0.3 - 0.4	1.5 - 2.5	$Im(\mathcal{A})$

Table 6: Main features of SPD-related experiments in the world. The status column indicates whether the data is published (pub.), preliminary (prelim.), the experiment is approved (approv.), proposed (prop.) or under study (study.). The luminosity $\mathcal{L}$ is in units of cm^{-2}s^{-1}. The exclusivity column (exclus.) states whether or not the experimental setup can check the exclusivity of the reaction. The letter $\mathcal{A}$ represents the amplitude of the measured process.

13 Summary and Conclusion

We have shown that it is possible to study the DVCS process at Jefferson Lab using a 6 GeV polarized electron beam, the Hall A liquid hydrogen cryotarget, a dedicated photon calorimeter and a recoil proton detector. The triple coincidence is an important feature of this experiment, since we make sure of the exclusivity of the events.

Counting rates in the calorimeter as well as electron-photon coincidence **accidentals rates have been estimated and are manageable** at a luminosity of 10^{37} cm^{-2}s^{-1}. The addition of the proton detector will further enhance our trues to falses ratio. A test run aimed to measure counting rates in the proton detector as well as in the calorimeter will take place before PAC18.

By measuring the difference in cross-section for electrons of opposite helicities, we are able to extract the imaginary part of the DVCS amplitude. By studying its Q^2 behavior, it is possible to look for the **onset of handbag diagram dominance**. Due to its close relationship with the deep inelastic scattering (via the optical theorem), the imaginary part of the DVCS amplitude is expected to scale as early as Q^2=1 GeV^2. Assuming we reach this regime, we will be able to extract the **skewed parton distributions contribution to the imaginary part of the DVCS amplitude** for the

first time. We will also be able to separately estimate the size of the **higher twist terms in the DVCS process**, only suppressed by an additional $1/Q$ factor compared to the leading twist term.

The time estimates are given below for each kinematic setting and include calibrations. These were determined assuming a beam polarization of 70 % and a luminosity of 10^{37} cm^{-2}s^{-1} corresponding to a $3\mu A$ beam impinging on the 15 cm liquid hydrogen target. The beam time request seems reasonable considering the uncertainty in the SPD models and in our luminosity limitations at this time.

s GeV^2	Q^2 GeV^2	$-t$ GeV^2	time hours
5.5	2.5	0.15/0.45	200
4.5	2.0	0.15/0.30	200
3.5	1.5	0.15/0.30	200
Total beam request:			600

Table 7: Beam time request for each kinematic point at fixed $x_B \approx 0.35$. The values of $-t$ are the minimum and maximum within the acceptance.

14 Acknowledgment

We are especially grateful to M. Diehl, B. Pire and A.V. Radyushkin for their most valuable theoretical expertise on the matter of SPD's, and for taking the time to answer all our questions.

A DVCS formalism and notations

In this appendix we present the basic formalism of Deeply Virtual Compton Scattering. We use the notation of Ji [10], Guichon and Vanderhaeghen [18].

For explicitness, we work in a reference frame in which the virtual photon $\vec{q}$ and the average nucleon 3-vector $P = (p + p')/2$ are both along the z-axis. We define the two light cone vectors

$$\tilde{p}^\mu = \frac{\Lambda}{\sqrt{2}}(1, 0, 0, 1) \quad \& \quad n^\mu = \frac{1}{\Lambda\sqrt{2}}(1, 0, 0, -1). \tag{4}$$

Boosts along the z-axis simply change the value of Λ. The light cone vectors satisfy the identities:

$$\tilde{p} \cdot \tilde{p} = n \cdot n = 0 \quad \& \quad \tilde{p} \cdot n = 1. \tag{5}$$

In the following, we choose a boost such that

$$\Lambda = P^+ = P \cdot n. \tag{6}$$

Denoting the x-, y-components with the T subscript, the kinematic vectors can be decomposed as follows

$$\begin{aligned} P^\mu &= \tilde{p}^\mu + n^\mu \left(\overline{M}^2/2\right), \\ \overline{M}^2 &= P^2 = M^2 + t/4, \qquad (7) \\ q^\mu &= \tilde{p}^\mu(-2\xi') + n^\mu Q^2/(4\xi'), \\ \Delta^\mu &= q^\mu - q'^\mu = p'^\mu - p^\mu = -2\xi\tilde{p}^\mu + \xi\overline{M}^2 n^\mu + \Delta_T^\mu \qquad (8) \end{aligned}$$

The variables ξ and ξ' are [one half] the light cone momentum fractions of Δ and q, respectively:

$$\begin{aligned} 2\xi' = -q^+ = -q \cdot n &= \frac{P \cdot q}{\overline{M}^2}\left[-1 + \sqrt{1 + \frac{Q^2\overline{M}^2}{(P \cdot q)^2}}\right] \xrightarrow{\text{Bj}} \frac{x_B}{1 - x_B/2} \\ 2\xi = -\Delta^+ = -\Delta \cdot n &= 2\xi' \frac{Q^2 + t}{Q^2 + \overline{M}^2(2\xi')^2} \xrightarrow{\text{Bj}} \frac{x_B}{1 - x_B/2} \end{aligned} \tag{9}$$

In the Bjorken limit of high Q^2 and finite x_B, to leading order in $1/Q^2$, the DVCS amplitude is given by the 'handbag' amplitude of Fig. 1b (+ crossed diagram):

$$\begin{aligned} \mathcal{T}^{\text{DVCS}} &= \epsilon^*_{f\mu} H^{\mu\nu}_{\text{DVCS}} j_\nu / q^2 \\ & \quad H^{\mu\nu}_{\text{DVCS}} = H^{\mu\nu}_V + H^{\mu\nu}_A \qquad (10) \\ H^{\mu\nu}_V &= \frac{1}{2}\left[\tilde{p}^\mu n^\nu + n^\mu \tilde{p}^\nu - g^{\mu\nu}\right] \int_{-1}^{+1} dx \left[\frac{1}{x - \xi + i\eta} + \frac{1}{x + \xi - i\eta}\right] \\ & \quad n_\kappa \overline{U}(p') \left[\gamma^\kappa H(x, \xi, t) + \frac{i\sigma^{\kappa\lambda}\Delta_\lambda}{2M} E(x, \xi, t)\right] U(p) \qquad (11) \\ H^{\mu\nu}_A &= \frac{-i}{2}\epsilon^{\mu\nu\kappa\lambda}\tilde{p}_\kappa n_\lambda \int_{-1}^{+1} dx \left[\frac{1}{x - \xi + i\eta} - \frac{1}{x + \xi - i\eta}\right] \\ & \quad \overline{U}(p') \left[\gamma \cdot n\gamma_5 \widetilde{H}(x, \xi, t) - \gamma_5 \frac{\xi}{M} \widetilde{E}(x, \xi, t)\right] U(p). \qquad (12) \end{aligned}$$

The skewed parton distributions (SPD) $\mathcal{O} = H, E, \widetilde{H}, \widetilde{E}$ have a flavor dependence:

$$\mathcal{O} = \sum_f q_f^2 \mathcal{O}_f(x, \xi, t) \tag{13}$$

The SPD's H and E are, respectively, the helicity-conserving and helicity-flip light cone matrix elements of the vector current, whereas $\widetilde{H}$ and $\widetilde{E}$ are the helicity-conserving and helicity-flip light cone matrix elements of the axial current:

$$\frac{1}{2\pi}\int d(y\cdot\tilde{p})e^{-x(y\cdot\tilde{p})}\left\langle p'\right|\psi_f(-y/2)\gamma\cdot n\psi_f(y/2)\left|p\right\rangle_{(y\cdot n)=\vec{y}_T=0} = \\ \overline{U}(p')\left[\gamma\cdot n\ H_f(x,\xi,t)+\frac{in_\kappa\sigma^{\kappa\lambda}\Delta_\lambda}{2M}E_f(x,\xi,t)\right]U(p) \tag{14}$$

$$\frac{1}{2\pi}\int d(y\cdot\tilde{p})e^{-x(y\cdot\tilde{p})}\left\langle p'\right|\psi_f(-y/2)\gamma\cdot n\gamma_5\psi_f(y/2)\left|p\right\rangle_{(y\cdot n)=\vec{y}_T=0} = \\ \overline{U}(p')\left[\gamma\cdot n\gamma_5\widetilde{H}_f(x,\xi,t)+\gamma_5\frac{\Delta\cdot n}{2M}\widetilde{E}_f(x,\xi,t)\right]U(p). \tag{15}$$

A prominent feature which distinguishes the SPD's from the (forward) parton distributions is the skewedness (ξ) dependence. As the (electron helicity) cross-section difference accesses the SPD along the line $x=\xi$, *e.g.* $H(\xi,\xi=x,t)$, one can compare this function with the one which one obtains using a factorized ansatz for the SPD's, proportional to the forward quark distribution *e.g.* $q(x)\cdot F(t)$. This is shown in Fig. 13 for the valence down contribution to the SPD H, by comparing the factorized calculation with a ξ dependent model [36]. The ξ dependence leads to an enhancement of the asymmetry. Therefore, this asymmetry provides a rather sensitive observable of the ξ dependence of the SPD's.

B Skewed parton distributions relations and sum rules

In the forward direction ($\xi=t=0$), the SPD's H and $\widetilde{H}$ reduce to the usual parton distributions $q(x)$ and $\Delta q(x)$:

$$H^q(x,\xi=0,t=0) = q(x)\,, \tag{16}$$

$$\widetilde{H}^q(x,\xi=0,t=0) = \Delta q(x)\,, \tag{17}$$

where the q stands for the quark flavor[3].

By integrating equations 14 and 15 over x, one gets the following relations between the first moments of the SPD's and the elastic form factors (for each quark flavor)

$$\int_{-1}^{+1}dxH^q(x,\xi,t) = F_1^q(t)\,,\quad \int_{-1}^{+1}dxE^q(x,\xi,t)=F_2^q(t)\,, \tag{18}$$

$$\int_{-1}^{+1}dx\widetilde{H}^q(x,\xi,t) = g_A^q(t)\,,\quad \int_{-1}^{+1}dx\widetilde{E}^q(x,\xi,t)=h_A^q(t)\,, \tag{19}$$

where F_1^q and F_2^q are the Dirac and Pauli form factors, g_A^q is the axial form factor and h_A^q is the induced pseudoscalar form factor. Note that the ξ dependence drops out in the previous equations.

The second moment of the SPD's is relevant to the nucleon spin structure. It was shown in Ref. [10] that there exists a gauge-invariant decomposition of the nucleon spin:

$$\frac{1}{2}=J_q+J_g\,, \tag{20}$$

where J_q and J_g are respectively the total quark and gluon spin contributions to the nucleon spin and can be decomposed in a spin part $\Delta\Sigma$ and an orbital momentum part L_q as follows:

$$J_q=\frac{1}{2}\Delta\Sigma+L_q\,. \tag{21}$$

[3]Just like for usual parton distributions, the SPD's are defined for each flavor. Measurements on different targets would be necessary to separate the different flavor contributions.

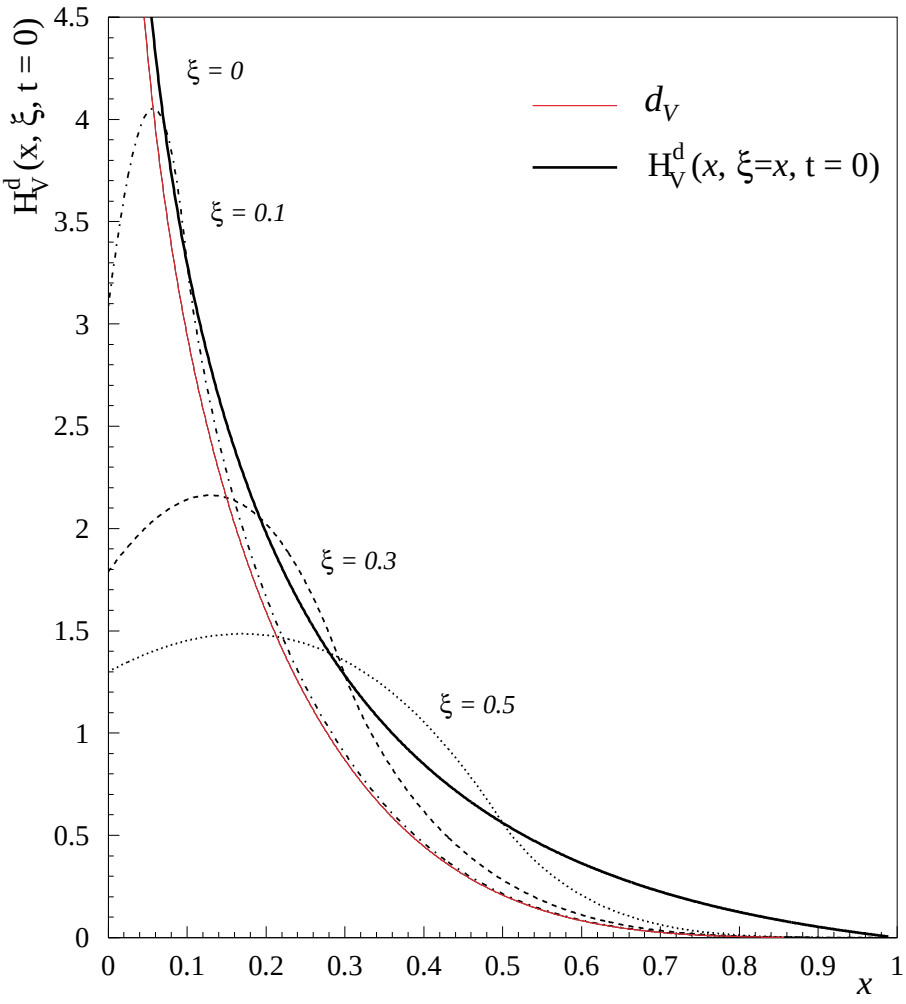

Figure 13: Valence down quark contribution to the SPD H as a function of x for different values of ξ (thin solid line: $\xi = 0$, dot-dashed line: $\xi = 0.1$, dashed line: $\xi = 0.3$, dotted line: $\xi = 0.5$). Also we have plotted the envelope function $H_V^d(x, \xi = x, t = 0)$ in thick solid line, accessible through the imaginary part of the DVCS amplitude. One must note that $H_V^d(x, \xi = 0, t = 0)$ (thin solid line) corresponds to the valence down quark distribution in the proton d_V (*cf.* next section). Those curves are based on a factorized ansatz and use the MRST98 parametrization of parton distributions.

The second moment of the SPD's gives:

$$\frac{1}{2}\int_{-1}^{+1} dx\, x[H(x,\xi,t=0)+E(x,\xi,t=0)] = J_q\,. \tag{22}$$

One must remember that $\Delta\Sigma$ is constrained in DIS experiments. Therefore, if one makes enough measurements to extract the second moments of the SPD's, the sum rule will determine the quark orbital momentum contribution to the nucleon spin[4].

C Helicity amplitudes

The full $ep \to ep\gamma$ cross-section can be written as

$$\begin{aligned}
-s'u'\left.\frac{d\sigma}{d\varphi\, dt\, dQ^2\, dx_B}\right|_I &= \frac{\alpha_{em}^3}{8\pi}\frac{1}{E_{lab}^2}\frac{1}{x_B^2\sqrt{2(1-x_B)(1+4x_B^2M_p^2/Q^2)}}\frac{Q^3}{M_p\, t} \\
&\times e_\ell\,\frac{\epsilon}{1-\epsilon}\left[\cos\varphi\,\frac{1}{\sqrt{\epsilon(1-\epsilon)}}\,\mathrm{Re}\,\widetilde{M}^{1,\,1} - \cos 2\varphi\,\sqrt{\frac{1+\epsilon}{1-\epsilon}}\,\mathrm{Re}\,\widetilde{M}^{0,\,1}\right. \\
&\qquad - \cos 3\varphi\,\sqrt{\frac{\epsilon}{1-\epsilon}}\,\mathrm{Re}\,\widetilde{M}^{-1,\,1} \\
&\left. + P_\ell\left\{-\sin\varphi\,\sqrt{\frac{1+\epsilon}{\epsilon}}\,\mathrm{Im}\,\widetilde{M}^{1,\,1} + \sin 2\varphi\,\mathrm{Im}\,\widetilde{M}^{0,\,1}\right\} + O\left(\frac{1}{Q}\right)\right],
\end{aligned} \tag{23}$$

where $e_\ell = \pm 1$ is the lepton charge in units of the positron charge e, and P_ℓ is the longitudinal lepton beam polarization (ranging from -1 to 1). E_{lab} denotes the lepton beam energy in the target rest frame, M_p the proton mass and ϵ is the degree of polarization of the virtual photon. The proton helicity averaged amplitudes are given by:

$$\begin{aligned}
\widetilde{M}^{\lambda',\lambda}(Q^2,x_B,\Delta_T) &= \frac{\Delta_T}{M_p}\left[(1-x_B)G_M - (1-x_B/2)F_2\right]\mathcal{M}^{\lambda',\lambda}_{-1/2,-1/2} \\
&+ \frac{\Delta_T}{M_p}\left[G_M - (1-x_B/2)F_2\right]\mathcal{M}^{\lambda',\lambda}_{1/2,1/2} \\
&+ \left[x_B^2 G_M + \frac{\Delta_T^2}{2M_p^2}F_2\right]\mathcal{M}^{\lambda',\lambda}_{-1/2,1/2} \\
&- \frac{\Delta_T^2}{2M_p^2}F_2\mathcal{M}^{\lambda',\lambda}_{1/2,-1/2} + O(\frac{1}{Q})
\end{aligned} \tag{24}$$

In this expression G_M and F_2 are the magnetic and Pauli elastic form factors of the proton evaluated at the transfer -t.

These amplitudes can be expressed with the conventional notation

$$\begin{aligned}
\mathcal{M}^{1,1}_{+1/2,+1/2} &= \Phi_1 \\
\mathcal{M}^{1,1}_{-1/2,-1/2} &= \Phi_5 \\
\mathcal{M}^{1,1}_{-1/2,+1/2} &= \Phi_4 \\
\mathcal{M}^{1,1}_{+1/2,-1/2} &= \Phi_8 \\
\mathcal{M}^{1,0}_{+1/2,+1/2} &= \Phi_9
\end{aligned} \tag{25}$$

[4]We have to stress that it is not the goal of this proposal to extract this kind of information. It has taken deep inelastic scattering experiments almost 20 years to measure $\Delta\Sigma$ to a still limited accuracy.

$$
\begin{aligned}
\mathcal{M}^{1,0}_{-1/2,-1/2} &= -\Phi_{11} \\
\mathcal{M}^{1,0}_{-1/2,+1/2} &= \Phi_{12} \\
\mathcal{M}^{1,0}_{+1/2,-1/2} &= \Phi_{10} \\
\mathcal{M}^{1,-1}_{+1/2,+1/2} &= \Phi_{7} \\
\mathcal{M}^{1,-1}_{-1/2,-1/2} &= \Phi_{3} \\
\mathcal{M}^{1,-1}_{-1/2,+1/2} &= -\Phi_{6} \\
\mathcal{M}^{1,-1}_{+1/2,-1/2} &= -\Phi_{2}
\end{aligned}
$$

The difference in cross-section for electrons of opposite helicities can be expressed in function of the helicity amplitudes as follows:

$$
\begin{aligned}
&\frac{d^5\ \overrightarrow{\sigma}}{dQ^2 dx_B dt d\varphi} - \frac{d^5\ \overleftarrow{\sigma}}{dQ^2 dx_B dt d\varphi} \\
&= \frac{1}{s'u'} \sum_{i=1}^{13} \Phi_i \left[a_i(\epsilon, Q^2, x_B, t) \sin\varphi + b_i(\epsilon, Q^2, x_B, t) \sin 2\varphi + c_i \sin 3\varphi \right]
\end{aligned}
\tag{26}
$$

the Φ_i for i=1,12 corresponds to the usual notation for the helicity amplitudes *e.g.* [18]. We have defined Φ_{13} to be the contribution coming from the $|VCS|^2$ term. It is given by :

$$
\Phi_{13} = \sum_{\mu',\mu} Im \left\{ (\mathcal{M}^{1,1}_{\mu',\mu})^* \mathcal{M}^{1,0}_{\mu',\mu} - (\mathcal{M}^{1,-1}_{\mu',\mu})^* \mathcal{M}^{1,0}_{\mu',\mu} \right\} \tag{27}
$$

This contribution is present in the $\sin\varphi$, $\sin 2\varphi$ and $\sin 3\varphi$ terms. We have plotted in Fig. 14 the size of the kinematic coefficients a_i, b_i and c_i in front of $\sin\varphi$, $\sin 2\varphi$ and $\sin 3\varphi$ respectively. As we expected, the $\sin\varphi$ contribution is dominant. However, there is a contribution coming from the $\mathcal{M}^{1,0}_{\mu',\mu}$

If one measures the size of the $\sin 2\varphi$ contribution, one will have access to these terms as they are dominant in the $\sin 2\varphi$ behavior. One will be able to subtract their contribution from the $\sin\varphi$ part.

The $|VCS|^2$ contribution is expected to be suppressed. Not only are its coefficients relatively small as seen in Fig. 14, but in addition it is a product of two VCS amplitudes, one being $\mathcal{M}^{1,0}_{\mu',\mu}$ and thus, non-leading twist, *cf.* eq. 27.

The expression of A,B or C in terms of the SPD's can be worked out from the above formulas. For example, A is obtained by using Eq. 27 and Eq. 24. The result is, up to $O(1/Q)$ corrections and omits an explicit kinematical factor

$$
A \propto Im\widetilde{M}_{1,1} \tag{28}
$$

At leading twist and leading order in α_s, the handbag amplitudes for the DVCS are given by [37]

$$
\begin{aligned}
\mathrm{Re}\,\mathcal{M}^{1,1}_{\mu',\mu} &= -\sum_q e_q^2 \left[P \int_{-1}^{1} dx \left(\frac{1}{x-\xi} + \frac{1}{x+\xi} \right) A^q_{\mu',\mu}(x,\xi,t) \right. \\
&\qquad \left. + P \int_{-1}^{1} dx \left(\frac{1}{x-\xi} - \frac{1}{x+\xi} \right) \widetilde{A}^q_{\mu',\mu}(x,\xi,t) \right] \\
\mathrm{Im}\,\mathcal{M}^{1,1}_{\mu',\mu} &= \pi \sum_q e_q^2 \left[A^q_{\mu',\mu}(\xi,\xi,t) - A^q_{\mu',\mu}(-\xi,\xi,t) \right. \\
&\qquad \left. + \widetilde{A}^q_{\mu',\mu}(\xi,\xi,t) + \widetilde{A}^q_{\mu',\mu}(-\xi,\xi,t) \right],
\end{aligned}
\tag{29}
$$

where the sum runs over quark flavors with charge e_q in units of e, and P denotes Cauchy's principal value. $\mathcal{M}^{1,1}_{\mu',\mu}$ is obtained by changing the signs of all terms with $\widetilde{A}$; all other helicity amplitudes cancel.

For the different proton helicity transitions we have

$$\begin{aligned}
A^q_{+,+} &= \sqrt{1-\xi^2}\left[H^q - \frac{\xi^2}{1-\xi^2}E^q\right] \\
A^q_{-,-} &= A^q_{+,+} \\
A^q_{-,+} &= \frac{\Delta_T}{2M_p\sqrt{1-x_B}}E^q \\
A^q_{+,-} &= -A^q_{-,+} \\
\widetilde{A}^q_{+,+} &= \sqrt{1-\xi^2}\left[\widetilde{H}^q - \frac{\xi^2}{1-\xi^2}\widetilde{E}^q\right] \\
\widetilde{A}^q_{-,-} &= -\widetilde{A}^q_{+,+} \\
\widetilde{A}^q_{-,+} &= \frac{\Delta_T}{2M_p\sqrt{1-x_B}}\xi\widetilde{E}^q \\
\widetilde{A}^q_{+,-} &= \widetilde{A}^q_{-,+}\,. \qquad (30)
\end{aligned}$$

where ξ is the usual skewdness parameter, related to x_B in the Bjorken limit by $\xi = x_B/(2-x_B)$. Note that in the previous expressions, Δ_T is defined in the center of mass of the $\gamma^* p$ system.

Using Eq. 29 along with Eq. 30 and inserting into Eq. 24, one obtains the expression for A in terms of the SPD's:

$$A = \frac{\Delta_T}{2m}\sqrt{1-x_b}\left(F_1\mathcal{H}_1 + (F_1+F_2)\xi\widetilde{\mathcal{H}}_1 - \frac{t}{4M_p^2}F_2\mathcal{E}_1\right) \qquad (31)$$

where $\mathcal{H}_1$, $\mathcal{E}_1$ and $\widetilde{\mathcal{H}}_1$ are given by

$$\mathcal{H}_1 = \pi\sum_q e_Q^2(H(\xi,\xi,t) - H(-\xi,\xi,t)) \qquad (32)$$

$$\mathcal{E}_1 = \pi\sum_q e_Q^2(E(\xi,\xi,t) - E(-\xi,\xi,t)) \qquad (33)$$

$$\widetilde{\mathcal{H}}_1 = \pi\sum_q e_Q^2(\widetilde{H}(\xi,\xi,t) + \widetilde{H}(-\xi,\xi,t)) \qquad (34)$$

The summations over $x=\xi$ and $x=-\xi$ in the previous expressions correspond to summations over quarks and antiquarks. At small t, the kinematical factor in front of $\mathcal{E}_1$ is small. Therefore A is essentially a combination of $\mathcal{H}$ and $\widetilde{\mathcal{H}}$.

If we study the φ behavior, we will be able to access the A and B terms. There are definite predictions for the scaling behavior of these terms A and B. One of the goals of our experiment is to study their Q^2 dependence.

In the handbag approximation, the $\mathcal{M}^{1,0}_{\mu',\mu}$ terms vanish, thus the measurement of B will give us a signal for the handbag dominance. We expect the ratio $M^{1,0}/M^{1,1}$ (that is, B/A) to decrease as $1/Q^n$, $n \geq 1$ as we approach the handbag dominance region [17]. The term B is sensitive to higher twist effects, without being masked by a leading twist piece.

D Fast ADC sampling system

The maximum luminosity one can run the present proposal at is limited mostly by the counting rates in the calorimeter and the proton detector. The usual technique consisting of using a gated ADC after a photomultiplier can only accomodate a few % of pile-up. Moreover, when the amount of pile-up becomes large, both the energy and position resolutions start to degrade. This difficulty can be overcome if one directly digitizes pulses out of the photomultiplier, and separates the piled-up events.

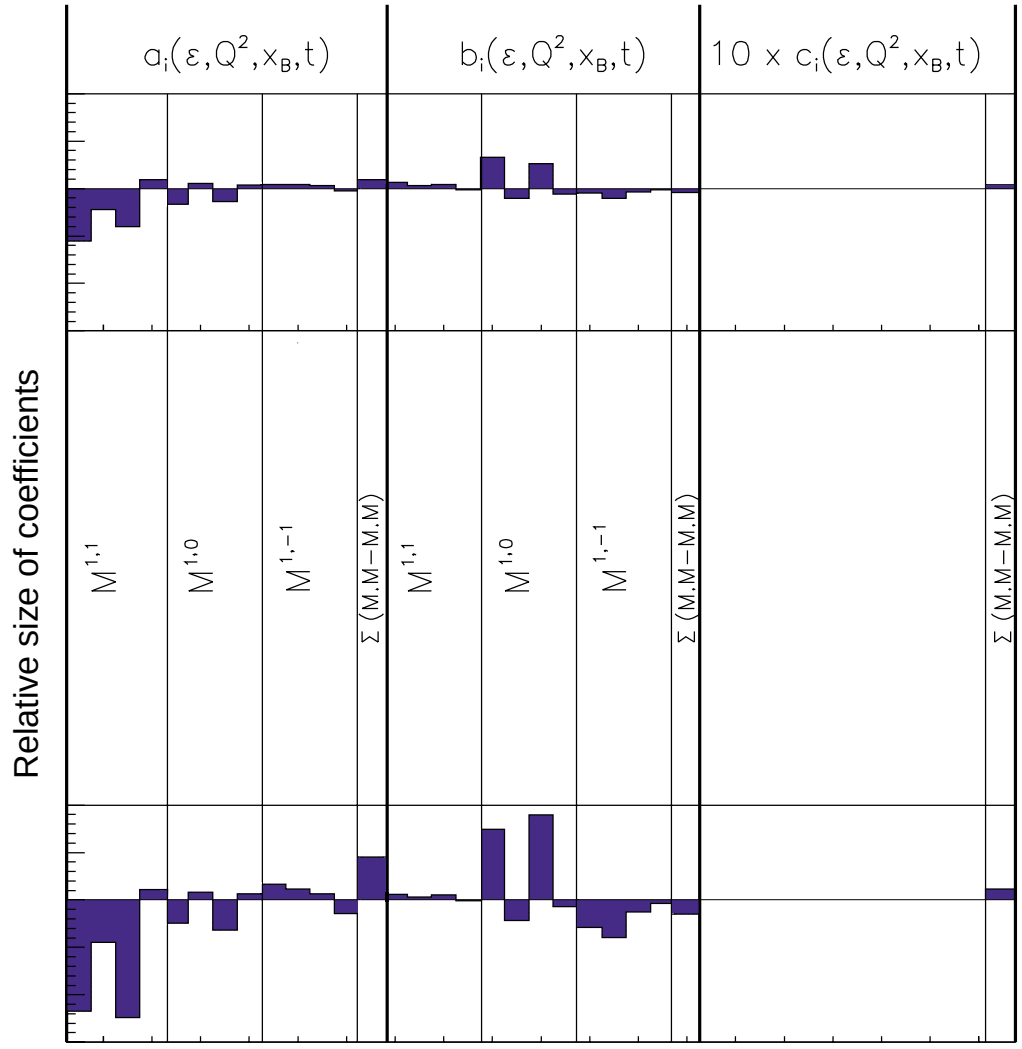

Figure 14: Size of the a_i,b_i and c_i coefficients in front of the of the helicity amplitudes for the $\sin\varphi$, $\sin 2\varphi$ and $\sin 3\varphi$ terms. The upper plots are for s=5.5 GeV^2, Q^2=2.5 GeV^2, the lower plots are for s=3.5 GeV^2, Q^2=1.5 GeV^2. The coefficients (from left to right) are in the order of Eq. 26. Note that the coefficient corresponding to $i = 13$ has a special meaning (see Eq. 27).

We propose to use a pulse shape analysis of each calorimeter and proton detector channel, with a 1 GHz sampling, during up to 256 ns. The device will use a pre-trigger at a rate of 1 MHz and will allow one to acquire events in coincidence with the HRSe spectrometer at a rate of ∼1 kHz. Such a system is currently being prototyped at LPC Clermont-Ferrand by P.Y. Bertin, M. Brossard and J. Lecoq.

D.1 Principle

D.1.1 Analog Memory Sampler: ARS

The core of the electronic circuit is the ARS, an Analog Memory Sampler. The ARS was developed by F. Feinstein and D. Lacharte from CEA Saclay [26] for the upcoming ANTARES experiment. The ARS is an array of 128 capacitor cells which sample and memorize the analog input signals at a frequency ranging from 300 MHz to 1 GHz. The ARS is composed of 5 coupled channels, which upon reception of a STOP signal, stops overwriting its cells. Each channel can then be read out at a rate of 6 kHz when the READ command is issued. The ARS is then set back in active mode through a RESET signal in less than 100 ns. The schematic of one ARS is shown in Fig. 15.

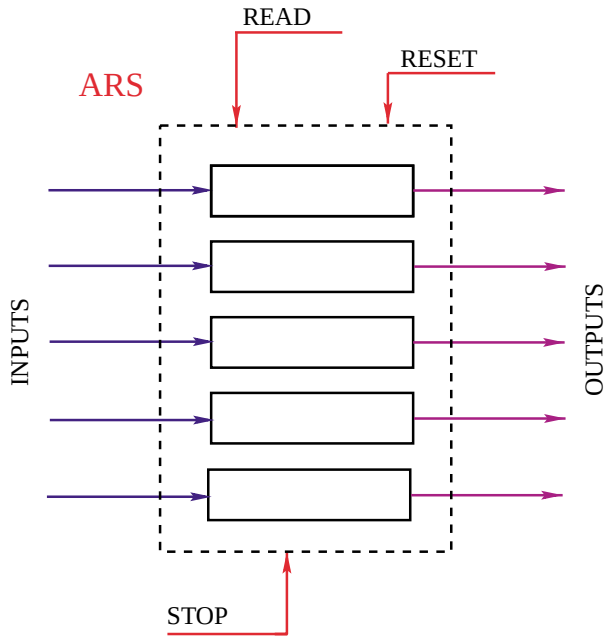

Figure 15: Schematic of an ARS circuit, which contains 5 analog memory samplers. The input is enabled through a RESET command. The STOP command stops the overwriting in the 128 analog memories. The samples are then extracted upon reception of the READ command.

Each analog output of a photomultiplier, labelled S_{xy} in the scope of this document, will be splitted and sent to two different ARS. This will allow to double the sampling duration from 128 to 256 ns. Of course, the first ARS will be stopped when the second ARS will start recording. The STOP signal for the second ARS is simply the STOP signal from the first, delayed by 128 ns.

D.1.2 Pretrigger

We propose to add a pretrigger to the ARS in order to:

- Define "virtual towers" of 9 blocks around the central block (coordinates x and y) which was hit by a particle.

- Build the sum of the analog signals of the 9 blocks E_{xy} that compose the virtual tower. This implies that each photomultiplier analog output has to be splitted into 9 (to allow the sum with all possible neighbors plus itself). Each of these signals then goes to adders, which will perform the analog sum.
- Build a logical Σ_{xy} signal by comparing E_{xy} with a given threshold via a comparator.
- Stop the overwriting of all ARS circuits associated with the virtual towers for which E_{xy} is above threshold.
- Build for each ARS a T_{xy} coincidence signal (level 2) between at least 1 of the 4 towers associated with that ARS and the spectrometer trigger signal T_e.
  - This signal will activate the extraction of the 4 ARS associated with the virtual tower,
  - it will reset the ARS if no coincidence of level 2 has been found.

A schematic of the pretrigger is given in Fig. 16 and 17. Figure 18 shows a schematic of the ARS

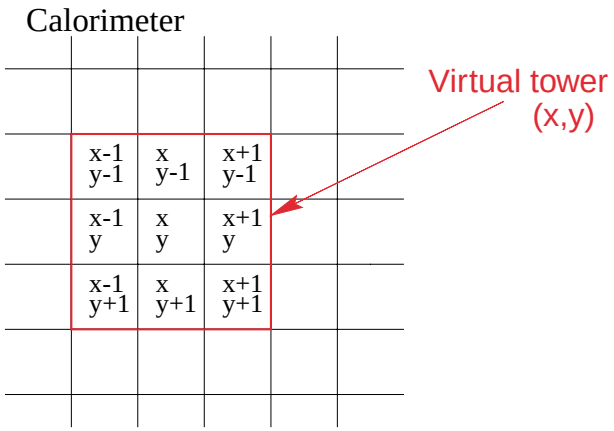

Figure 16: Definition of a virtual tower at coordinates (x, y) in the calorimeter, composed of 9 blocks (the central block + the first ring around it).

circuit for 9 blocks.

This system has been studied in a simulation. Fig. 19 shows both the efficiency of the pretrigger and the average multiplicity of virtual towers that triggered, as a function of the energy threshold. We have used in this simulation a relative energy resolution of $\sigma_E/E = 0.03 + 0.05/\sqrt{E}$.

This study show that the pretrigger efficiency will be 100% with a threshold set to 3/4 of the photon energy.

D.1.3 Timing calibration

A 20 MHz sine wave signal will be sent directly to one dedicated channel in each ARS as a time-stamp. One special ARS will be dedicated to put the T_e signal and the 20 MHz reference signal in phase.

D.1.4 Amplitude calibration

The gain of the electronics chain will be adjusted by varying the high voltage on each photomultiplier. It will be necessary to carefully adjust those gains in order to be able to perform meaningful sums of the signals in the pretrigger.

The calibration of the calorimeter will be achieved using an external light source, cosmic rays, or even physics events.

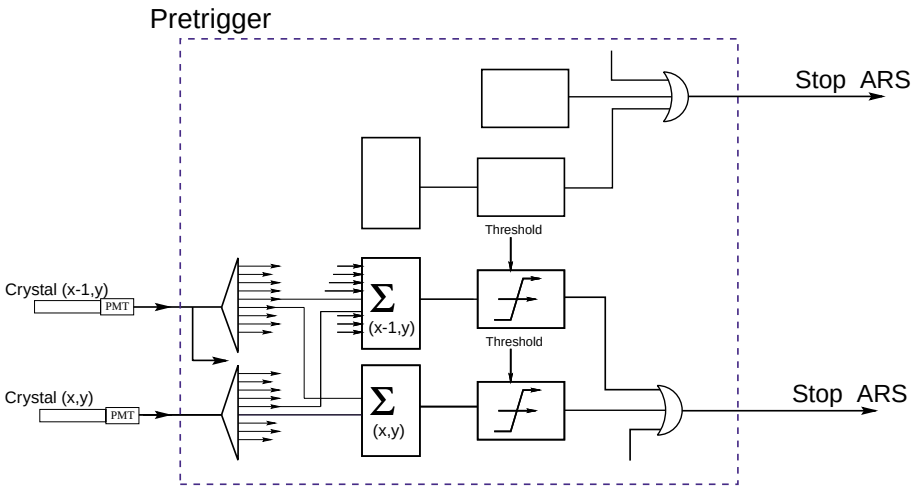

Figure 17: Schematic of the pretrigger. Each photomultiplier signal is split into 9 signals to participate to 9 possible virtual towers. The sum of 9 blocks composing each virtual tower is then compared to a given threshold in a comparator. A logical signal is formed and will eventually participate in a coincidence with the HRSe.

D.1.5 Data acquisition

As stated in section D.1.2, the readout of the 4 ARS associated with one virtual tower on an event by event basis will be triggered by the T_{xy} signal. The five channels of each ARS will be encoded in parallel with 5 decoders (10 bits) and buffered before they are sent to the data acquisition system. The total encoding time will be 166 μs.

D.1.6 Dead time

This device has several advantage compared to a conventional gated ADC technique:

- There is no need to delay the signals of the calorimeter to wait for the HRSe information. The signals will not be degraded by integration over a long cable (about 100 m/500 ns).
- The pretrigger dead time will be kept to a minimum. Only signals belonging to the towers in the cluster will be read. in the worst case, 25 channels will have signals above threshold. These channels will be reset very fast if no coincidence is found with the HRSe. If the singles rate in the calorimeter is such that 1 MHz of events have deposited enough energy to reach the threshold, the resulting deadtime will only be about 10%.
- The size of the transmitted data per event will be small compared to the potential amount of information: $25 \times 2 \times 128 \times 10$ bits = 60 kbits. The acquired information will be limited to the towers above threshold and the time-stamp.
- Due to the limited size of data to be transfered, the only limitation in the acquisition will come from the encoding time.

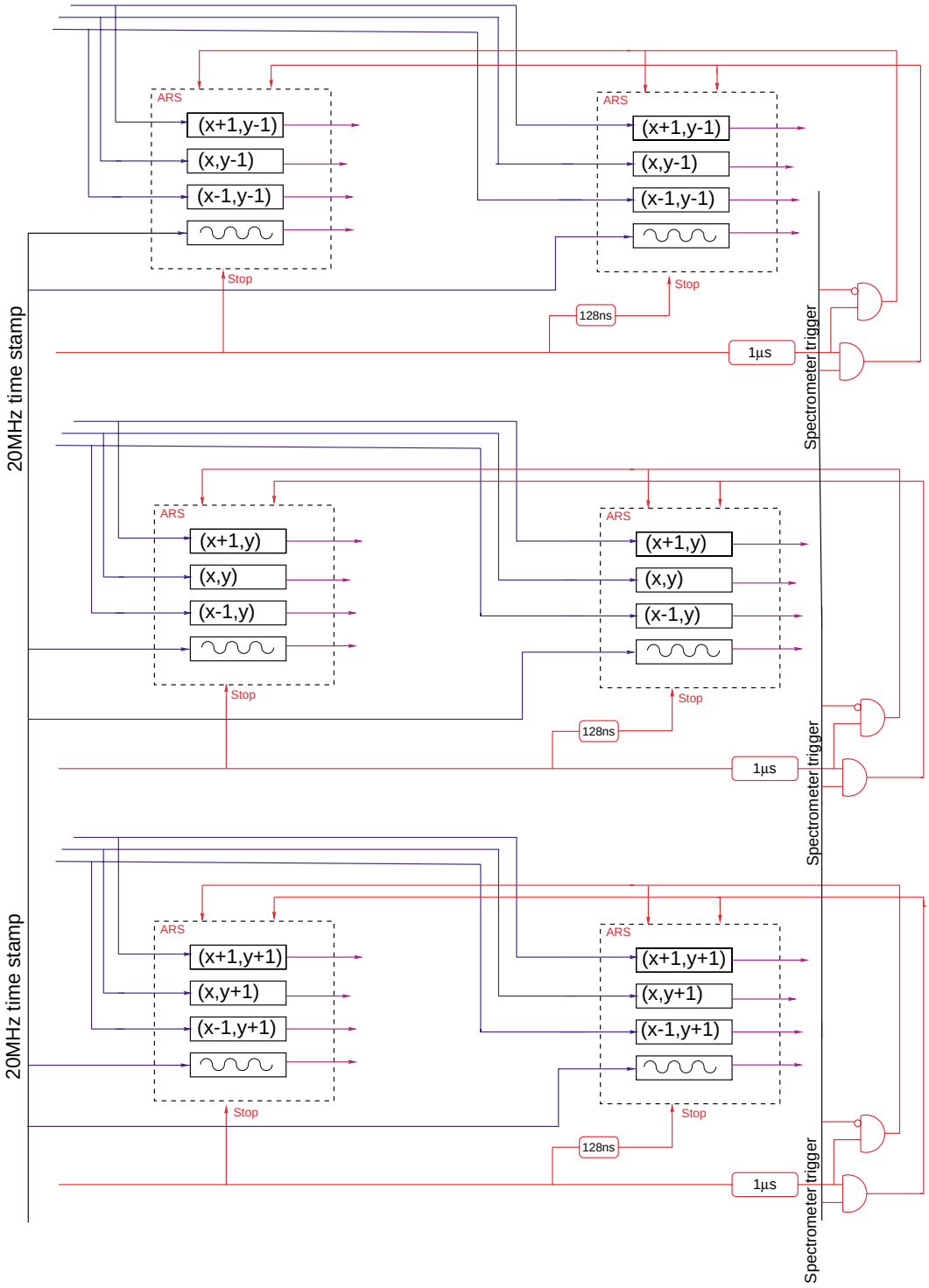

Figure 18: Six ARS circuits are used to digitize signals from 9 calorimeter blocks. In each ARS, a channel is used as a time-stamp with a common 20 MHz sine wave signal. Note that only 4 channels in each ARS is shown in that figure, but all 5 will be effectively used.

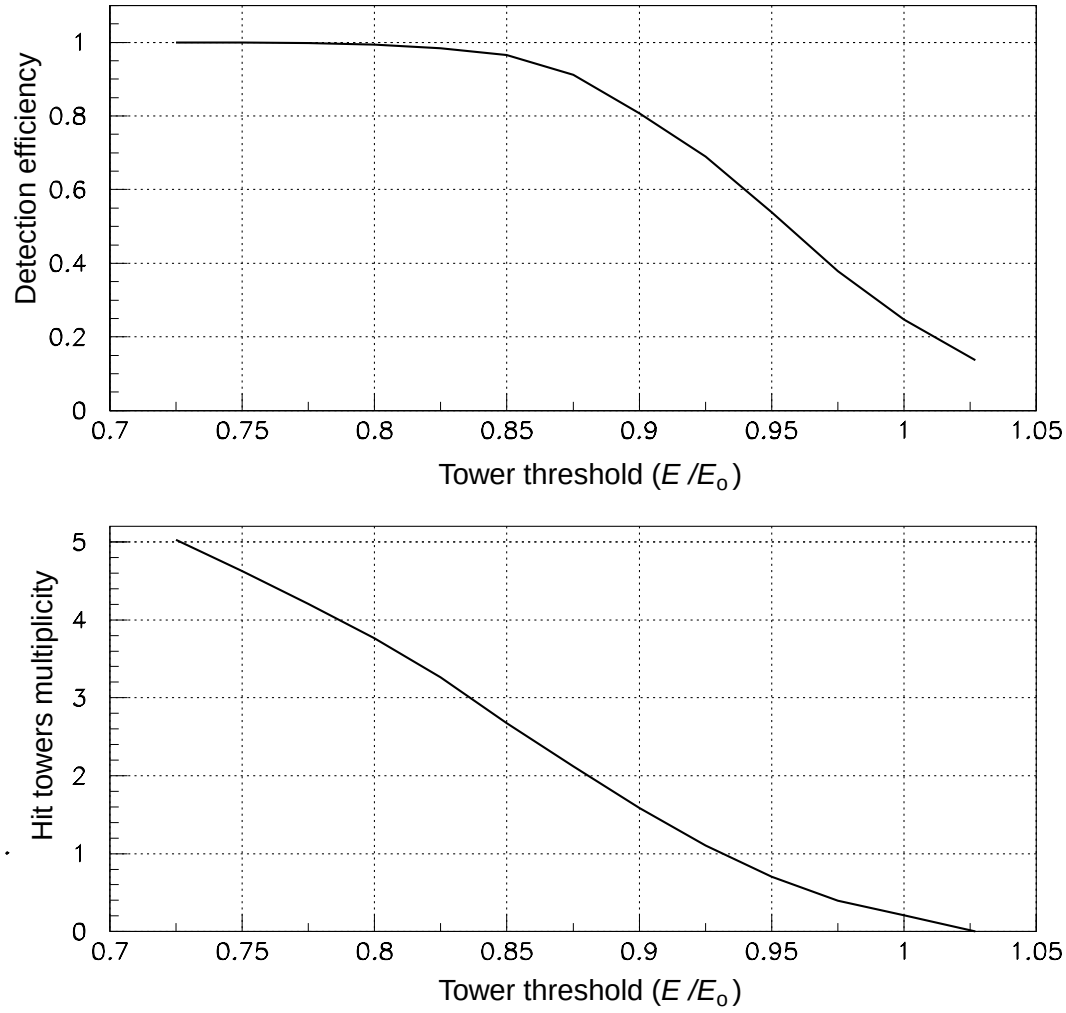

Figure 19: Detection efficiency of the pretrigger (top) and multiplicity of fired towers (bottom) versus threshold of the pretrigger.

References

[1] R. Hofstadter, *Ann. Rev. Nucl. Sci.* **7**, 231 (1958)
M. Jones *et al.*, *Phys. Rev. Lett.* **84**, 1398 (2000).

[2] I. Passchier *et al.*, *Phys. Rev. Lett.* **82**, 4988 (1999)
D. Rohe *et al.*, *Phys. Rev. Lett.* **83**, 4257 (1999).

[3] K. Aniol *et al.*, *Phys. Rev. Lett.* **82**, 1096 (1999)
D. Spayde *et al.*, *Phys. Rev. Lett.* **84**, 1106 (2000).

[4] J. Friedman ad H. Kendall, *Ann. Rev. Nucl. Sci.* **22**, 203 (1972).

[5] K. Abe *et al.*, *Phys. Lett.* **B364**, 61 (1995)
K. Abe *et al.*, *Phys. Rev. Lett.* **79**, 26 (1997)
P. Anthony *et al.*, *Phys. Lett.* **B463**, 339 (1999).

[6] D. Adams *et al.*, *Phys. Lett.* **B396**, 338 (1997)
D. Adams *et al.*, *Phys. Rev.* **D56**, 5330 (1997).

[7] D. Drell and T. Yan, *Phys. Rev. Lett.* **25**, 316 (1970).

[8] J. Collins and A. Freund, *Phys. Rev.* **D59**, 074009 (1999).

[9] J. Collins, L. Frankfurt and M. Strikman, *Phys. Rev.* **D56**, 2982 (1997).

[10] X. Ji, *Phys. Rev. Lett* **78**, 610 (1997)
X. Ji, *Phys. Rev.* **D55**, 7114 (1997).

[11] D. Müller *et al.*, *Fort. Phys.* **42**, 101 (1994).

[12] A.V. Radyushkin, *Phys. Lett.* **B380**, 417 (1996)
A.V. Radyushkin, *Phys. Lett.* **B385**, 333 (1996).

[13] Yu. L. Dokshitser, *Sov. Phys.* JETP **46**, 641 (1977)
G. Altarelli and G. Parisi. *Nucl. Phys* **B126**, 298 (1977)
L.N. Lipatov, *Sov. J. Nucl. Phys.* **20**, 94 (1975).

[14] G.P. Lepage and S.J Brodsky, *Phys. Lett.*, **B87**, 359 (1979)
A.V. Efremov and A.V. Radyuskin, *Phys. Lett.*, **B94**, 245 (1980).

[15] A.V Belitsky *et al.*, *Phys. Lett.*, **B474**, 163 (2000).

[16] S.J. Brodsky, F. Close, J.F. Gunion, *Phys. Rev.* **D6**, 177 (1972).

[17] M. Diehl *et al.*, *Phys. Lett.* **B411**, 183 (1997).

[18] P.A.M. Guichon and M. Vanderhaeghen, *Prog. Part. Nucl. Phys* **41**, 125 (1998).

[19] I.V. Musatov and A.V. Radyushkin, *Phys. Rev.* **D61**, 74027 (2000).

[20] M. Penttinen, M.V. Polyakov and K. Goeke, **hep-ph/9909489**.

[21] M.V. Polyakov and C. Weiss, *Phys. Rev.* **D60**, 114017 (1999).

[22] L. Mankiewicz, G. Piller and T. Weigl, *Eur. Phys. J.* **C5**, 119 (1998)

[23] X. Ji *et al.*, *Phys. Rev.* **D56**, 5511 (1997).

[24] Jefferson Lab experiment E-99114 in Hall A, *http://www.jlab.org/˜sabatie*.

[25] S. Incerti, Ph.D. Thesis, Université Blaise Pascal, Clermont-Ferrand, not published.

[26] F. Feinstein and D. Lachartre, "Specification of Front-End digital electronics for ANTARES detector", DAPNIA/CEA internal report, 1996.

[27] L.L. Frankfurt *et al.*, *Phys. Rev. Lett.* **84**, 2589 (2000)

[28] M. Vanderhaeghen, Private Communication.

[29] RCS internal report, "Study of Hall A photon spectrometer, results from test-runs July-August 1999" (1999).

[30] M. Vanderhaeghen *et al.*, **hep-ph/0001100** and *Phys. Rev. C*, In press.

[31] P.V. Degtyarenko, M.V. Kossov and H.-P. Wellisch, "Chiral Invariant Phase Space Event Generator", to be published in E.P.J.A.M

[32] N. d'Hose *et al.*, "Letter-of-Intent: DVCS at COMPASS", DAPNIA-CSTS-99, december 1999.

[33] A. Airapetian *et al.*, **DESY-00-058**, 2000. and **hep-ex/0004023**

[34] M. Guidal *et al.*, Jefferson Lab experiment E-99105 proposal, 1999.

[35] P.R.B. Saull *et al.*, **hep-ex/0003030**

[36] M. Vanderhaeghen, P.A.M. Guichon and M. Guidal, *Phys. Rev.* **D60**, 094017 (1999).

[37] M. Diehl, Private Communcation.

[38] P.Y. Bertin, Y. Roblin and C.E. Hyde-Wright, Fizika **B8**, 207 (1999).